FZD-519

Evolution of Ion-Induced Ripple Patterns

- Anisotropy, nonlinearity, and scaling

Adrian Keller

Juli 2009

Wissenschaftlich-Technische Berichte
FZD-519 2009 · ISSN 1437-322X

WISSENSCHAFTLICH-TECHNISCHE BERICHTE

Forschungszentrum
Dresden Rossendorf

Wissenschaftlich-Technische Berichte
FZD-519
Juli 2009

Adrian Keller

Evolution of Ion-Induced Ripple Patterns
- Anisotropy, nonlinearity, and scaling

Forschungszentrum
Dresden Rossendorf

Evolution of Ion-Induced Ripple Patterns

– Anisotropy, nonlinearity, and scaling

Dissertation

zur Erlangung des akademischen Grades

Doctor rerum naturalium
(Dr. rer. nat.)

vorgelegt
der Fakultät Mathematik und Naturwissenschaften
der Technischen Universität Dresden

von

Adrian Keller
geboren am 05.02.1981 in Coburg

Gutachter: Prof. Dr. W. Möller, FZ Dresden-Rossendorf
Prof. Dr. M. Springer, HS Coburg
Prof. Dr. R. Cuerno, Universidad Carlos III de Madrid

Eingereicht am: 10. März 2009
Tag der Verteidigung: 8. Juni 2009

The most exciting phrase to hear in science,
the one that heralds new discoveries,
is not 'Eureka!' but 'That's funny...'
–Isaac Asimov

There's real *poetry in the* real *world.*
Science is the poetry of reality.
–Richard Dawkins

All science is either physics
or stamp collecting.
–Ernest Rutherford

Abstract

This thesis addresses the evolution of nanoscale ripple patterns on solid surfaces during low-energy ion sputtering. Particular attention is paid to the long-time regime in which the surface evolution is dominated by nonlinear processes. This is explored in simulation and experiment.

In numerical simulations, the influence of anisotropy on the evolution of the surface patterns in the anisotropic stochastic Kuramoto-Sivashinsky (KS) equation with and without damping is studied. For a strong nonlinear anisotropy, a 90° rotation of the initial ripple pattern is observed and explained by anisotropic renormalization properties of the anisotropic KS equation. This explanation is supported by comparison with analytical predictions. In contrast to the isotropic stochastic KS equation, interrupted ripple coarsening is found in the presence of low damping. This coarsening seems to be a nonlinear anisotropy effect that occurs only in a narrow range of the nonlinear anisotropy parameter.

Ex-situ atomic force microscopy (AFM) investigations of Si(100) surfaces sputtered with sub-keV Ar ions under oblique ion incidence show the formation of a periodic ripple pattern. This pattern is oriented normal to the direction of the ion beam and has a periodicity well below 100 nm. With increasing ion fluence, the ripple pattern is superposed by larger corrugations that form another quasi-periodic pattern at high fluences. This ripple-like pattern is oriented parallel to the direction of the ion beam and has a periodicity of around one micrometer. Interrupted wavelength coarsening is observed for both patterns. A dynamic scaling analysis of the AFM images shows the appearance of anisotropic scaling at large lateral scales and high fluences. Based on comparison with the predictions of different nonlinear continuum models, the recent hydrodynamic model of ion erosion, a generalization of the anisotropic KS equation, is considered as a potentially powerful continuum description of this experiment.

In further *in-situ* experiments, the dependence of the dynamic scaling behavior of the sputtered Si surface on small variations of the angle of incidence is investigated by grazing incidence small angle X-ray scattering (GISAXS). A transition from strongly anisotropic to isotropic scaling is observed. This indicates the presence of at least two fixed points in the system, an anisotropic and an isotropic one. The dynamic scaling exponents of the isotropic fixed point are in reasonable agreement with those of the Kardar-Parisi-Zhang (KPZ) equation. It remains to be seen whether the hydrodynamic model is able to show such a transition from anisotropic to isotropic KPZ-like scaling.

Contents

Chapter 1

Introduction

Back in the 1960s, Navez *et al.* studied the morphology of glass surfaces bombarded with a 4 keV ion beam of air [1]. During the sputtering, they found the surface to develop periodic structures with lateral dimensions ranging from 30 to 120 nm depending on the angle of incidence. The orientation of the structures was determined by the direction of the ion beam. For grazing incidence, ripple patterns oriented parallel to the projection of the ion beam were observed whereas the ripples were rotated by 90° at near-normal incidence. At normal incidence, however, the surface developed dot-like features. In the following years, sputter-induced ripple structures were found on all kinds of amorphous as well as crystalline materials like insulators [2], semiconductors [2,3], and metals [4].

During the 1990s, several *in-* and *ex-situ* studies investigated the ion-induced formation of nanoripples by means of new techniques for the exact characterization of the eroded surfaces like light scattering [5] and x-ray methods [6], as well as scanning tunneling [7] and atomic force microscopy [8]. In 1999, Facsko *et al.* observed the formation of hexagonally ordered nanodots on GaSb surfaces during normal incidence ion sputtering [9]. Such regular dot patterns have been found on various semiconductor surfaces sputtered at normal incidence [10] as well as off-normal incidence with [11] and without sample rotation [12].

Nowadays, ion-induced nanopatterns become interesting for certain technological applications. Recent experiments demonstrate the principal applicability of nanoripples in the fabrication of microelectronic devices [13] and optically active nanostructure arrays [14,15]. Another approach uses nanodot formation under normal incidence sputtering of layer stacks to create isolated magnetic islands for magnetic storage media [16,17].

In addition, rippled substrates are becoming popular as templates for thin film deposition. It was shown that nanorippled substrates induce additional magnetic anisotropies in ultrathin single-crystalline [18] and poly-crystalline [19] metal films. Moreover, the self-organized alignment of physical-vapor deposited metal nanoparticles on nanorippled substrates was recently observed, leading to large arrays of nanoparticle chains exhibiting polarization-dependent plasmon absorption [20]. With the same technique, also arrays of metallic nanowires could be produced [21]. Most of these applications crucially depend on certain properties of the template patterns such as a high degree of order in the case of storage media [16] or a well defined ripple wavelength that fits to the growth conditions of the nanoparticles [20]. A precise control of the pattern properties in turn requires detailed knowledge of the pattern formation process and the contributing mechanisms. Up to now, however, this knowledge is still incomplete.

Although several possible origins of the ripple patterns like ion-induced local stresses or initial surface defects have been suggested in the years following their discovery [3], no conclusive explanation could be found until 1988. In this year, Bradley and Harper developed a continuum model [22] to describe the formation of the ripple patterns based on the so-called micro-roughening instability [23]. It was already shown by Sigmund [23] that the local erosion rate of a surface under ion bombardment is higher in depressions than on elevations. This curvature dependence of the sputter yield induces an instability of the surface against periodic disturbances which leads to an amplification of all initial modulations. In the presence of a competing smoothing process like surface self-diffusion, however, a wavelength selection is observed with the most unstable mode growing the fastest [22].

The resulting linear continuum equation, the so-called Bradley-Harper (BH) equation, is able to reproduce some of the main experimentally observed features of the formation and early evolution of the patterns like their orientation with respect to the ion beam and the exponential growth of the ripple amplitude. For long sputtering times, however, certain experimental observations such as the saturation of the ripple amplitude cannot be explained within the framework of the linear model. This disagreement was attributed to a growing influence of nonlinear terms that dominate the morphology at later times. Hence, in 1995, Cuerno and Barabási derived a nonlinear continuum equation of the Kuramoto-Sivashinsky (KS) type to describe the ion-induced formation of periodic surface structures [24]. In the early time regime, this equation behaves like the linear BH equation. At a certain transition time, however, the nonlinear terms start to control the evolution of the surface [25]. When entering this nonlinear regime, the amplitude of the ripples saturates as observed experimentally. However, a transition to kinetic roughening with a loss of lateral order is observed in this regime [25, 26]. Whereas such a transition has been observed in a few experiments [27], other studies report a stabilization of the regular patterns at high fluences [28, 29]. Another feature of the experimental pattern evolution that could not be reproduced by the KS equation is the occasionally observed coarsening of the pattern wavelength [8, 10, 11, 30–33]. In order to overcome these discrepancies, several other nonlinear models based on the KS equation have been proposed [34–38]. These models all show a similar behavior in their linear regime and make different predictions only for the surface evolution in the nonlinear regime corresponding to rather long sputter times. Therefore, a distinct demand for high fluence experiments has developed which investigate the evolution of the surface morphology in the nonlinear regime in order to identify the continuum model that describes the given experimental system.

A common way to identify the proper continuum model for describing an interface during a certain growth or erosion process is the analysis of its dynamic scaling behavior [39]. In many cases, an evolving surface exhibits spatial and temporal fluctuations that follow certain scaling relations similar to those observed in equilibrium critical phenomena [40, 41]. Thus, similar to the case of equilibrium systems, critical scaling exponents can be determined in surface growth or erosion that then characterize the rough surface in space and time. Based on the determined scaling exponents, a particular growth or erosion system can be assigned to a certain universality class and, therefore, to a certain (linear or nonlinear) continuum equation that is able to describe the given system [39].

In the case of surface erosion by ion sputtering, however, this dynamic scaling approach is hindered by the fact that most of the current nonlinear continuum equations show a rather complex behavior and exhibit a truly rich parameter space. Therefore, although their general ability to describe ion-induced pattern formation has been demonstrated, the detailed behavior of the different models in the nonlinear regime is yet to be investigated. Even basic properties like the number of fixed points and the value of the corresponding critical scaling exponents are often not definitely known [42]. Especially when it comes to anisotropic systems (corresponding to oblique ion incidence), these models become even more complex due to the increased number of parameters and are, therefore, usually even less studied. Nevertheless, experimental studies that explore the nonlinear regime and investigate the dynamic scaling behavior of the surface in detail provide important insight in the formation mechanism and yield information about the relevance of the single linear and nonlinear terms that may or may not contribute to the surface evolution. This way, experimentally determined scaling exponents are important for the verification of current or future continuum models. On the other hand, also further systematic numerical investigations of the nonlinear surface evolution in the different continuum models, especially in the anisotropic case, are needed in order to map the behavior of these equations in parameter space. This can prove useful for the explanation of some recent and rather peculiar experimental observations like the appearance of ordered dot patterns under oblique ion incidence [12, 43] or the rotation of ripple patterns with increasing fluence [44].

In this work, the nonlinear evolution of nanoscale ripple patterns induced by low-energy ion sputtering has been investigated in simulation and experiment. Chapter 2 summarizes the theoretical basics of ion sputtering and ion-induced pattern formation. It also provides an overview of the various continuum equations currently available to describe the formation and evolution of regular patterns during ion sputtering. Chapter 3 is devoted to the nonlinear morphology evolution in the anisotropic KS equation. The stochastic anisotropic KS equation with and without damping has been integrated numerically and different aspects of the surface morphology, namely the rotation of the ripple patterns and the coarsening of the ripple wavelength have been studied. Chapter 4 provides a brief overview of the dynamic scaling concept in surface growth and erosion. The experimental methods for sample preparation and characterization are described in chapter 5. In chapter 6, the nonlinear regime of the pattern evolution during high-fluence sub-keV ion sputtering of silicon is explored *ex-situ* and *in-situ* by atomic force microscopy and X-ray scattering, respectively. From these measurements, the coarsening of the ripples as well as the dynamic scaling behavior of the surface morphology is evaluated and compared to the predictions of different nonlinear continuum models. The last chapter gives some final remarks and conclusions.

Chapter 2

Ion-induced Pattern Formation

If a solid surface is bombarded with energetic ions, surface material will be removed. This mechanism is called *sputtering*. The ions penetrating into the target surface are slowed down and lose their kinetic energy and momentum in elastic and inelastic collisions with target nuclei and electrons, respectively. For kinetic energies below 1 keV as used in the experiments of this work, however, the momentum and kinetic energy of the ions is transferred to the target atoms in nuclear collisions mainly and inelastic collisions play only a minor role [45]. A target atom taking part in one of these collisions receives some of the ion's kinetic energy and momentum and can, therefore, be set in motion. If such an atom receives enough energy, it can induce further collisions with other target atoms, thus increasing the number of moving atoms. This situation is then called collision cascade [45]. For typical ion fluxes, the collision cascades do not overlap in space and time and can therefore be treated independently. Within one collision cascade, it may happen that a target atom receives momentum directed towards the surface. If the kinetic energy of such an atom is high enough to overcome the surface binding energy, it will leave the surface and be sputtered away. Under continuous irradiation, the surface will be eroded as a whole.

When bombarding a crystalline non-metallic surface, e.g. a semiconductor, one can observe an additional effect. The number of generated defects in the crystal increases with the number of ion impacts. Therefore, for a large number of ion impacts, the crystal structure of the surface becomes unstable and the whole surface gets amorphized [45]. For single crystalline Si surfaces bombarded at energies of a few hundred eV at room temperature, this amorphisation is observed already after the impact of about 10^{15} ions per cm^2 [45]. For higher fluences, the surface can be treated as fully amorphous.

2.1 Sigmund's theory of sputtering

A sub-keV ion penetrating a solid surface loses its kinetic energy mainly in nuclear collisions with target atoms. The energy loss per unit path length, or stopping power, is then given by

$$\frac{dE}{dz} = -NS_n(E) \tag{2.1}$$

with the atomic density N of the solid and the nuclear stopping cross section $S_n(E)$. E is the initial kinetic energy of the penetrating ion.

The nuclear stopping cross section $S_n(E)$ depends on the interaction potential used to model the collision between ion and target atom. With the power approximation of the Thomas-Fermi potential as a common choice, $S_n(E)$ reads [46]

$$S_n(E) = \frac{1}{1-m} C_m \omega^{1-m} E^{1-2m}. \tag{2.2}$$

Here, m accounts for the Coulomb screening of the nuclei due to the electrons in the solid and ranges from 0 to 1. In the lower-keV and upper eV region, $m = 1/3$ is commonly assumed, whereas m should be close to zero in the eV region [46]. C_m and ω are constants that incorporate the atomic parameters of the projectile and target species:

$$\begin{aligned} C_m &= \frac{\pi}{2}\lambda_m a_{TF}^2 \left(\frac{M_p}{M_t}\right)^m \left(\frac{2Z_pZ_te^2}{a_{TF}}\right)^{2m}, \\ \omega &= \frac{4M_pM_t}{(M_p+M_t)^2}. \end{aligned} \tag{2.3}$$

$M_{p,t}$ is the atomic mass and $Z_{p,t}$ the atomic number of the projectile and the target atom, respectively. λ_m is a dimensionless function of m with values ranging from $\lambda_1 = 0.5$ to $\lambda_0 \sim 24$ and a_{TF} is the Thomas-Fermi screening length.

The average number of sputtered atoms per incident ion is given by the sputtering yield Y. For linear collision cascades, i.e. for a sufficiently small number and isotropic distribution of binary collisions within one cascade [45], the sputtering yield Y is proportional to the energy $F_D(z)$ deposited per unit depth in the surface at $z = h$ by a certain ion at the lateral position (x, y),

$$Y(E, \theta, x, y) = \Lambda F_D(E, \theta, x, y, z = h) \tag{2.4}$$

with the ion energy E and the angle of incidence θ. Λ is given by

$$\Lambda = \frac{\Gamma_m}{8(1-2m)} \frac{1}{NC_m E_{sb}^{1-2m}}. \tag{2.5}$$

Here, E_{sb} is the surface binding energy and Γ_m a function of m given by

$$\Gamma_m = \frac{m}{\frac{d}{dx}[\ln \Gamma(x=1)] - \frac{d}{dx}[\ln \Gamma(x=1-m)]}. \tag{2.6}$$

Because the majority of the sputtered particles originates from secondary collisions with low energy (< 50 eV) recoils, Sigmund suggested $m = 0$ for equation (2.5) [46], resulting in $\Gamma_0 = 6/\pi^2$. Therefore, equation (2.5) becomes

$$\Lambda = \frac{3}{4\pi^2} \frac{1}{NC_0 E_{sb}}, \tag{2.7}$$

with $C_0 = 0.0181$ nm^2 [46].

For a plane and homogeneous surface, the deposited energy does not depend on the lateral position of the ion impact and is given by

$$F_D(E,\theta) = \alpha N S_n(E), \tag{2.8}$$

with α being a dimensionless function of the angle of incidence θ and the mass ratio M_t/M_p [46]. Then, the sputtering yield becomes

$$Y(E,\theta) = \frac{4.2}{\mathrm{nm}^2} \frac{\alpha S_n(E)}{E_{sb}}. \tag{2.9}$$

2.2 Sputtering of rough surfaces: the Bradley-Harper model

If a surface is bombarded with a homogeneous flux of ions j, then the over all energy deposited in a given point A of the surface is the sum of the energy deposited in this point due to all surrounding ion impacts. Therefore, with equation (2.4), the local erosion rate in point A is given by the integral over all contributing events [23]

$$v(A) = \frac{\Lambda}{N} \int \int \phi(\mathbf{r}) E_D(\mathbf{r}) \mathrm{d}x \mathrm{d}y \tag{2.10}$$

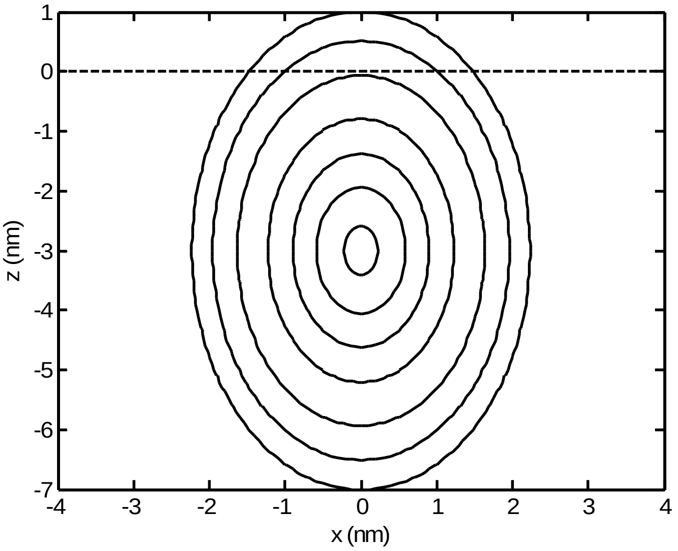

Figure 2.1: Contour plot of the deposited energy in the x-z plane according to equation (2.12) with $a = 3$ nm, $\sigma = 0.9$ nm, $\mu = 0.5$ nm, and $E = 500$ eV. The surface at $z = 0$ is indicated by the broken line.

where $\phi(\mathbf{r})$ is the flux of incoming ions j corrected for the local angle of incidence and $E_D(\mathbf{r})$ is the energy deposited per unit volume at $\mathbf{r} = (x, y, z)$. $E_D(\mathbf{r})$ is related to $F_D(z)$ of equation (2.4) by [23]

$$F_D(z) = \int\int E_D(\mathbf{r}) \mathrm{d}x \mathrm{d}y. \tag{2.11}$$

The spatial distribution of the deposited energy $E_D(\mathbf{r})$ can be approximated by a Gaussian,

$$E_D(\mathbf{r}) = \frac{E}{(2\pi)^{3/2}\sigma\mu^2} \exp\left(-\frac{(z+a)^2}{2\sigma^2} - \frac{x^2+y^2}{2\mu^2}\right). \tag{2.12}$$

Here, μ and σ represent the lateral and longitudinal width of the distribution, respectively, and a is the mean penetration depth of the ion. A contour plot of the energy distribution is shown in Fig. 2.1.

For a rough surface sputtered with an uniform flux of ions, the energy deposited in the surface is not constant but rather depends on the lateral position $\mathbf{r}$. To some extent, this is caused by the angular dependence of the ion flux at the surface. In addition, however, the energy deposition into the surface depends on the local shape of the surface. This

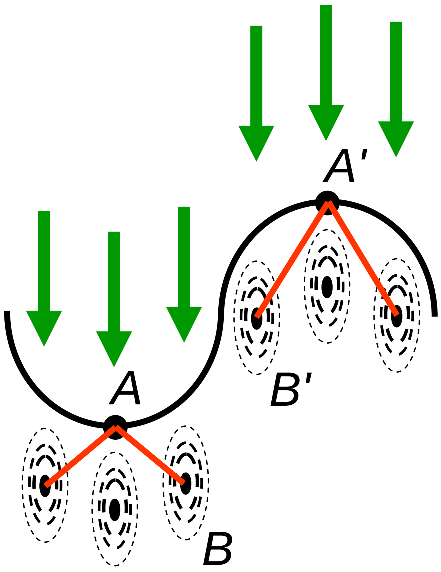

Figure 2.2: Schematic drawing of the energy deposition in rough surfaces, see text.

lateral variation of the energy deposition causes a lateral variation of the local erosion rate and, therefore, a change of the surface morphology with sputtering time [23]. A closer inspection of the underlying mechanisms reveals that the local erosion rate is higher in troughs than on crests. This is demonstrated in Fig. 2.2 where ions penetrate into a surface region with positive (Fig. 2.2 left) and negative (Fig. 2.2 right) curvature, respectively. The Gaussian distribution of the deposited energy is centered at the mean penetration depth a of the ions and indicated by the (broken) lines of constant energy. From Fig. 2.2 it is obvious that the distance from the surface point A where the sputtering occurs to the contributing impact at B is shorter than the distance $A' - B'$. Therefore, the over all deposited energy and also the erosion rate is larger in points with positive curvature (A) than in those with negative curvature (A'). Obviously, the surface becomes unstable and the initial surface roughness gets amplified. This mechanism is called *surface microroughening* [23].

In order to explain the formation of periodic ripple patterns during sputtering, Bradley and Harper have calculated the integral (2.10) under the assumption of large radii of curvature R_x and R_y [22]. Then, the time evolution of the continuous surface height function $h(x, y, t)$ is given by

$$\frac{\partial h}{\partial t} = -v(\varphi, R_x, R_y)\sqrt{1 + (\nabla h)^2} \tag{2.13}$$

with φ being the angle between the direction of the ion beam and local surface normal [24]. The projected direction of the ion beam is parallel to the x axis. Equation (2.13) can then be expanded in terms of derivatives of the surface height [24]. To first order in the surface curvature, Bradley and Harper obtained

$$\frac{\partial h}{\partial t} = -v_0 + \gamma \frac{\partial h}{\partial x} + \nu_x \frac{\partial^2 h}{\partial x^2} + \nu_y \frac{\partial^2 h}{\partial y^2}. \tag{2.14}$$

Here, v_0 is the erosion velocity of the planar surface, γ causes a lateral movement of the structures, and the micro-roughening instability is incorporated by the coefficients $\nu_{x,y}$. These coefficients are given by the following relations [34]:

$$\begin{aligned} v_0 &= Fc, && (2.15)\\ \gamma &= F\frac{s}{f^2}\left[a_\sigma^2 a_\mu^2 c^2 \left(a_\sigma^2 - 1\right) - a_\sigma^4 s^2\right], && (2.16)\\ \nu_x &= Fa\frac{a_\sigma^2}{2f^3}\left[2a_\sigma^4 s^4 - a_\sigma^4 a_\mu^2 s^2 c^2 + a_\sigma^2 a_\mu^2 s^2 c^2 + a_\mu^4 c^4\right], && (2.17)\\ \nu_y &= -Fa\frac{c^2 a_\sigma^2}{2f}, && (2.18) \end{aligned}$$

with

$$\begin{aligned} F &= \frac{jE\Lambda a}{\sigma\mu N\sqrt{2\pi f}} e^{-a_\sigma^2 a_\mu^2 c^2/2f}, && (2.19)\\ f &= a_\sigma^2 s^2 + a_\mu^2 c^2, \\ a_\sigma = \frac{a}{\sigma} \quad &, \quad a_\mu = \frac{a}{\mu}, \\ s = \sin\theta \quad &, \quad c = \cos\theta. \end{aligned}$$

When sputtering a surface at finite temperature, atoms will diffuse on the surface leading to a relaxation of the surface. This effect can be introduced by adding a term proportional to the fourth derivative of the surface height to equation (2.14), resulting in [22]

$$\frac{\partial h}{\partial t} = -v_0 + \gamma \frac{\partial h}{\partial x} + \nu_x \frac{\partial^2 h}{\partial x^2} + \nu_y \frac{\partial^2 h}{\partial y^2} - K\nabla^4 h. \tag{2.20}$$

In the Bradley-Harper (BH) equation (2.20), K is the relaxation rate due to thermally activated surface self-diffusion [22],

$$K = \frac{D_s \varrho n_d}{N^2 k_B T}, \tag{2.21}$$

with the surface self-diffusivity D_s, the surface free energy per unit area ϱ, the areal density of diffusing atoms n_d, the Boltzmann constant k_B and the temperature T.

The behavior of equation (2.20) shall be analyzed by calculating its Fourier transform. Be $\tilde{h}(\mathbf{k}, t)$ the Fourier transform of the surface height function $h(\mathbf{r}, t)$ with the wave vector $\mathbf{k} = k_x \mathbf{e}_x + k_y \mathbf{e}_y$ and $\mathbf{r} = (x, y)$. Then, equation (2.20) can be written as

$$\frac{\partial \tilde{h}(\mathbf{k}, t)}{\partial t} = \left[- \left(\nu_x k_x^2 + \nu_y k_y^2 \right) - K \left(k_x^2 + k_y^2 \right)^2 \right] \tilde{h}(\mathbf{k}, t). \tag{2.22}$$

Integration of equation (2.22) yields

$$\tilde{h}(\mathbf{k}, t) = \tilde{h}_0(\mathbf{k}) \exp\left(R_k t \right), \tag{2.23}$$

with the growth rate $R_k = - \left[\nu_x k_x^2 + \nu_y k_y^2 + K \left(k_x^2 + k_y^2 \right)^2 \right]$. Therefore, spatial frequencies $\mathbf{k}$ with positive R_k grow exponentially in amplitude, whereas those with negative R_k decay exponentially with time. Because of the positive value of K, surface roughening occurs only for negative $\nu_{x,y}$. The maximum value of R_k is reached for

$$k_c = \sqrt{\frac{|\min\left(\nu_x, \nu_y \right)|}{2K}}. \tag{2.24}$$

Therefore, the Fourier component of the initial roughness spectrum with the wave number k_c will grow fastest, resulting in a wavelike surface pattern with a periodicity

$$\lambda = \frac{2\pi}{k_c} = 2\pi \sqrt{\frac{2K}{|\min\left(\nu_x, \nu_y \right)|}}. \tag{2.25}$$

For $\nu_x < \nu_y$ and $\nu_x > \nu_y$, the wave vector of the observed pattern is $\mathbf{k_c} = k_c \mathbf{e}_x$ and $\mathbf{k}_c = k_c \mathbf{e}_y$, respectively. The angular dependence of $\nu_{x,y}$ for a certain set of microscopic parameters is shown in Fig. 2.3. At an angle of $\theta \sim 70°$, one observes a change from $\nu_x < \nu_y$ to $\nu_x > \nu_y$ what corresponds to a rotation of the observed ripple pattern from normal to parallel with respect to the projected direction of the ion beam. Such a rotation has been observed in several experiments [1, 27, 30, 47, 48]. Some other predictions of the BH equation, however, are in contrast to certain experimental observations:

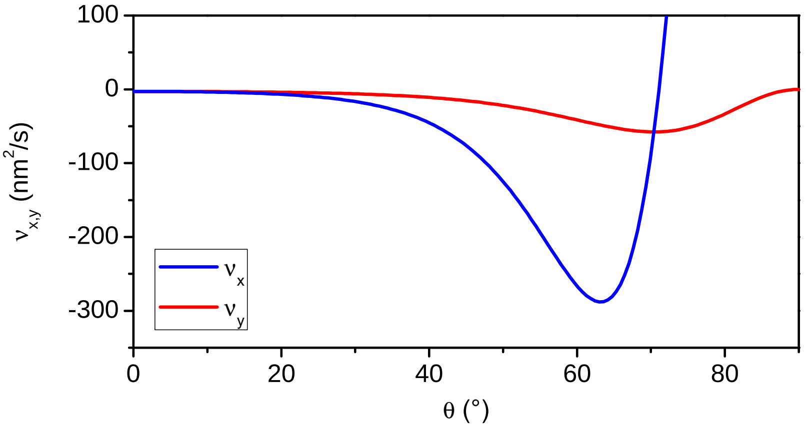

Figure 2.3: $\nu_{x,y}$ versus angle of incidence θ, calculated for 500 eV Ar$^+$ irradiation of Si with $j = 5 \times 10^{15}$ cm^{-2}s^{-1}, $a = 3$ nm, $\sigma = 0.9$ nm, $\mu = 0.7$ nm, and $Y = 3$.

- The amplitude of the ripples should grow exponentially without saturation. In experiments, however, saturation of the ripple amplitude at a constant value is observed after an initial exponential increase [49, 50].

- From equations (2.25), (2.17), and (2.18) it follows that $\lambda \propto j^{-1/2}$. In contrast, some experimental studies report the ripple wavelength λ to be constant with the ion flux j [51].

- Furthermore, from the same equations λ follows to be a function of the ion energy E and the penetration depth a, which again is a function of E. Therefore, one expects the ripple wavelength to decrease with the ion energy as $\lambda \propto E^{-p}$ [52]. However, this behavior is only observed at relatively high temperatures [53]. At low and moderate temperatures, several studies report the ripple wavelength to increase with energy [29, 54, 55].

- Equations (2.25) and (2.21) indicate a dependence of λ on the sample temperature. Again, such a dependence of the wavelength was only observed at elevated temperatures whereas λ was found to be constant at room temperature and below [56]. Another study found λ to be relatively constant with temperature even up to about

200°C [57].

- Equation (2.25) implies that the ripple wavelength λ is independent on the ion fluence Φ and should, therefore, be constant with sputtering time. Several experiments, however, show an increase of λ with fluence [8,30–33,44]. This phenomenon is usually referred to as *coarsening*.

Several attempts have been made in order to overcome these deficiencies of the BH equation and shall be discussed in the following.

2.3 Higher order extensions of the Bradley-Harper equation

2.3.1 Kuramoto-Sivashinsky equation

In the series expansion of equation (2.13), Bradley and Harper considered only linear terms. Cuerno and Barabási, however, took the expansion to lowest nonlinear order resulting in [24]

$$\begin{aligned} \frac{\partial h}{\partial t} &= -v_0 + \gamma \frac{\partial h}{\partial x} + \nu_x \frac{\partial^2 h}{\partial x^2} + \nu_y \frac{\partial^2 h}{\partial y^2} \\ &\quad + \frac{\zeta_x}{2} \left(\frac{\partial h}{\partial x} \right)^2 + \frac{\zeta_y}{2} \left(\frac{\partial h}{\partial y} \right)^2 - K \nabla^4 h + \eta. \end{aligned} \tag{2.26}$$

The additional nonlinear terms in this equation are nonconserved Kardar-Parisi-Zhang (KPZ) nonlinearities [39,58] that incorporate the dependence of the local erosion velocity on the absolute value of the surface slopes (not to be confused with the dependence on the local incident angle). Their coefficients are given by [34]

$$\begin{aligned} \zeta_x &= F \frac{c}{2f^4} \left[a_\sigma^8 a_\mu^2 s^4 \left(3 + 2c^2\right) + 4 a_\sigma^6 a_\mu^4 s^2 c^2 - a_\sigma^4 a_\mu^6 c^4 \left(1 + 2s^2\right) \right. \\ &\quad \left. - f^2 \left(2 a_\sigma^4 s^2 - a_\sigma^2 a_\mu^2 \left(1 + 2s^2\right)\right) - a_\sigma^8 a_\mu^4 s^2 c^2 - f^4 \right], \qquad (2.27) \\ \zeta_y &= F \frac{c}{2f^2} \left[a_\sigma^4 s^4 + a_\sigma^2 a_\mu^2 c^2 - a_\sigma^4 a_\mu^2 c^2 - f^2 \right]. \qquad (2.28) \end{aligned}$$

In order to account for the stochastic arrival of the ions, the Gaussian white noise term η, defined as

$$\langle \eta(\mathbf{r}, t) \eta(\mathbf{r}', t') \rangle = 2 D_\eta \delta^d(\mathbf{r} - \mathbf{r}') \delta(t - t'), \tag{2.29}$$

was added. Here, D_η is the strength of the noise and d the dimension of the surface.

Equation (2.26) is an anisotropic stochastic generalization of the so-called Kuramoto-Sivashinsky (KS) equation which was originally proposed to describe chemical waves [59] and the propagation of flame fronts [60]. For short sputtering times, this equation behaves like the linear BH equation with an exponential increase of the ripple amplitude and constant ripple wavelength. Then, at a certain transition time

$$t_c \propto \frac{K}{\nu_{x,y}^2} \ln\left(\frac{\nu_{x,y}}{\zeta_{x,y}}\right), \tag{2.30}$$

the surface enters a nonlinear regime and a saturation of the ripple amplitude as in the experiments is observed [25]. However, numerical analyses of the noisy KS equation in 1+1 and 2+1 dimensions show that the saturation of the ripple amplitude is accompanied by a transition to kinetic roughening [25, 26]. In this regime, the surface does not exhibit any lateral order.

In the asymptotic limit of long times and large lateral scales, the linear coefficients $\nu_{x,y}$ in equation (2.26) are assumed to renormalize to *positive* values [26, 42]. Then, the asymptotic behavior of equation (2.26) should be described by the anisotropic KPZ equation [26, 42, 58]

$$\frac{\partial h}{\partial t} = \nu_x^* \frac{\partial^2 h}{\partial x^2} + \nu_y^* \frac{\partial^2 h}{\partial y^2} + \frac{\zeta_x}{2}\left(\frac{\partial h}{\partial x}\right)^2 + \frac{\zeta_y}{2}\left(\frac{\partial h}{\partial y}\right)^2 + \eta \tag{2.31}$$

with $\nu_{x,y}^* > 0$. Although this renormalization has already been demonstrated for the KS equation in $1+1$ dimensions, it is not clear yet whether this assumption also holds in $2+1$ dimensions [42].

2.3.2 Damped Kuramoto-Sivashinsky equation

The KS equation is able to reproduce the observed saturation of the ripple amplitude. However, it also predicts a transition to kinetic roughening that (although observed in few experiments [27]) is in contrast to several experimental reports of a pattern conservation at high fluences [28, 29].

Inspired by the observation of stationary patterns in numerical simulations of the isotropic *damped* KS (dKS) equation by Paniconi and Elder [61], Facsko *et al.* adopted this equation for normal incidence ion sputtering [35]. The isotropic dKS equation is frequently used to describe different processes like compact electrodeposition growth [62] or directional solidification [61]. For oblique ion sputtering, however, the anisotropic dKS equation must be applied:

$$\begin{aligned}\frac{\partial h}{\partial t} &= -v_0 - \kappa h + \gamma\frac{\partial h}{\partial x} + \nu_x\frac{\partial^2 h}{\partial x^2} + \nu_y\frac{\partial^2 h}{\partial y^2} \\ &\quad + \frac{\zeta_x}{2}\left(\frac{\partial h}{\partial x}\right)^2 + \frac{\zeta_y}{2}\left(\frac{\partial h}{\partial y}\right)^2 - K\nabla^4 h + \eta. \qquad (2.32)\end{aligned}$$

This equation differs from the undamped KS equation (2.26) just by the additional damping term $-\kappa h$ with κ being a damping coefficient that enters the effective growth rate of the ripple amplitude $R^*_{k_c} = R_{k_c} - \kappa$. This damping term induces smoothing of all spatial frequencies and, therefore, prevents kinetic roughening.

In the case of sputter erosion, the damping term in equation (2.32) violates the translational invariance of the surface in the erosion direction. However, translational invariance can be restored by replacing the term $-\kappa h$ by $-\kappa(h - \bar{h})$ with $\bar{h}$ being the mean height of the surface and thus transforming equation (2.32) into a nonlocal dKS equation [35] which again, as has been demonstrated [63], can be exactly mapped to a local dKS equation. The physical meaning of κ, however, is still not clear in the case of sputter erosion.

The dKS equation has been extensively studied in numerical simulations [35, 63–66]. It is not only able to show stationary patterns in the long-time limit but also to reproduce other features of experimental patterns like certain pattern defects [35] or the formation of structured islands [66]. However, no evidence for wavelength coarsening as observed in several experiments [8, 10, 11, 30–33] has been found yet [65].

2.3.3 General continuum equation

Although equation (2.26) includes KPZ-like nonlinearities, other higher order terms are neglected [24]. The most general nonlinear equation that results from the expansion of equation (2.13) is given by [34]

$$\begin{aligned}\frac{\partial h}{\partial t} &= -v_0 + \gamma\frac{\partial h}{\partial x} + \sum_{i=x,y}\left\{-\nu_i\frac{\partial^2 h}{\partial i^2} + \zeta_i\left(\frac{\partial h}{\partial i}\right)^2 + \Omega_i\frac{\partial^2}{\partial i^2}\frac{\partial}{\partial x}h + \right. \\ &\quad \left. \xi_i\left(\frac{\partial h}{\partial x}\right)\left(\frac{\partial^2 h}{\partial i^2}\right)\right\} + \sum_{i,j=x,y}\left\{-D_{ij}\frac{\partial^2}{\partial i^2}\frac{\partial^2}{\partial j^2}h\right\} - K\nabla^4 h + \eta. \qquad (2.33)\end{aligned}$$

The coefficients of the additional linear and nonlinear terms then read

$$\begin{aligned}
\Omega_x &= -Fa^2 \frac{3}{6f^2} \frac{s}{a_\mu^2} \left[f^2 - f a_\sigma^4 c^2 - \left(a_\mu^2 - a_\sigma^2 \right) c^2 \left(f + a_\sigma^4 s^2 \right) \right], && (2.34) \\
\Omega_y &= Fa^2 \frac{1}{6f^4} \left[-3sf^2 \left(f + a_\sigma^4 s^2 \right) + a_\sigma^2 c^2 \left(3a_\sigma^2 sf + a_\sigma^6 s^3 \right) f \right. \\
&\quad \left. +2 \left(a_\mu^2 - a_\sigma^2 \right) c^2 \left(3f^2 s + 6a_\sigma^4 s^3 + a_\sigma^8 s^5 \right) \right], && (2.35) \\
\xi_x &= Fa \frac{a_\sigma^2 sc}{2f^5} \left[-6a_\sigma^8 s^6 + a_\sigma^8 a_\mu^2 s^4 \left(4 + 3c^2 \right) - a_\sigma^8 a_\mu^4 c^2 s^4 + a_\sigma^6 a_\mu^4 c^2 s^2 \left(4 - 6s^2 \right) \right. \\
&\quad + a_\sigma^6 a_\mu^2 s^4 \left(-3 + 15s^2 \right) + a_\sigma^4 a_\mu^4 3c^2 s^2 \left(4 + 3s^2 \right) \\
&\quad \left. - a_\sigma^4 a_\mu^6 3c^4 \left(1 + s^2 \right) + a_\sigma^2 a_\mu^6 c^4 \left(9 - 3s^2 \right) - 3a_\mu^8 c^6 \right], && (2.36) \\
\xi_y &= Fa \frac{a_\sigma^2 sc}{2f^3} \left[-a_\sigma^4 a_\mu^2 c^2 + a_\sigma^4 s^2 \left(2 + c^2 \right) - a_\mu^4 c^4 + a_\sigma^2 a_\mu^2 c^2 \left(3 - 2s^2 \right) \right] && (2.37) \\
D_{xx} &= F \frac{a^3}{24} \frac{1}{f^5} \left[-4 \left(3a_\sigma^2 s^2 f + a_\sigma^6 s^4 \right) f^2 + a_\sigma^2 c^2 \left(3f^2 + 6a_\sigma^4 s^2 f + a_\sigma^8 s^4 \right) f \right. \\
&\quad \left. +2 \left(a_\mu^2 + a_\sigma^2 \right) c^2 \left(15a_\sigma^2 s^2 f^2 + 10a_\sigma^6 s^4 f + a_\sigma^{10} s^6 \right) \right], && (2.38) \\
D_{yy} &= F \frac{a^3}{24} \frac{1}{f^5} \frac{3a_\sigma^2}{a_\mu^2} \left[f^4 c^4 \right], && (2.39) \\
D_{xy} &= F \frac{6a^3}{24} \frac{1}{f^5} \frac{f^2}{a_\mu^2} \left[-2 \left(a_\sigma^2 s^2 \right) f^2 + a_\sigma^2 c^2 \left(f^2 + a_\sigma^4 s^2 f \right) \right. \\
&\quad \left. +2 \left(a_\mu^2 - a_\sigma^2 \right) c^2 \left(3a_\sigma^2 s^2 f + a_\sigma^6 s^4 \right) \right]. && (2.40)
\end{aligned}$$

Actually, the ξ and Ω terms in equation (2.33) have already been derived in reference [24] but were neglected since their influence on the asymptotic scaling of the surface was assumed to be of minor importance. The terms with the coefficients D_{ij} enter equation (2.33) in the form of diffusion-like terms proportional to the fourth derivative of the height function and thus lead to an additional *anisotropic* smoothing of the surface. Therefore, this relaxation mechanism is usually called *effective* or *ion-induced surface diffusion* (ISD) [67]. However, it is important to note that ISD results from preferential erosion during the sputtering which appears as a reorganization of the surface and does *not* involve any mass transport along the surface. Thus, ISD is strictly speaking no diffusion mechanism. This is also displayed by the fact that the coefficient D_{xx} might even become negative at large incident angles, leading to an additional instability of the surface [67].

Since ISD does not depend on the temperature (cf. equations (2.38) - (2.40)), this smoothing mechanism is able to explain the temperature independence of the wavelength at low temperatures where thermal diffusion can be neglected. In this case, the ripple wavelength is given by

$$\lambda_{ISD} = 2\pi\sqrt{\frac{2D_{xx,yy}}{|\min(\nu_x,\nu_y)|}}. \tag{2.41}$$

From equations (2.17), (2.18), (2.38), and (2.41) it follows that the wavelength at low temperatures does no longer depend on the ion flux. Moreover, with $a \propto E^{2m}$ [45], we find $\lambda_{ISD} \propto E^p$ and, therefore, an increase of λ_{ISD} with the ion energy. At high temperatures, however, thermal diffusion becomes the dominating smoothing mechanism and the wavelength follows from equation (2.25). Hence, with the incorporation of ISD into equation (2.33), one is able to explain the experimentally observed flux and temperature independence of the wavelength, as well as its increase with ion energy. However, the fluence dependence of the ripple wavelength as observed in some experiments [8,30–33,44], still cannot be explained by the general continuum equation.

In the special case of normal ion incidence, the general continuum equation (2.33) is reduced to the isotropic stochastic KS equation with $\gamma = \xi_x = \xi_y = \Omega_x = \Omega_y = 0$, $\nu_x = \nu_y$, $\zeta_x = \zeta_y$, and $D_{xx} = D_{yy} = D_{xy}/2$. For off-normal incidence, however, equation (2.33) has a highly nonlinear character with a rich parameter space which might lead to rather complex morphologies and dynamic behaviors. Although some general features of equation (2.33) have been studied [34], its detailed behavior, and especially the role of the additional nonlinearities with the coefficients $\xi_{x,y}$, is still to be investigated.

2.3.4 Hydrodynamic model

In order to overcome the inability of the KS-type equations (2.26), (2.32), and (2.33) to predict ripple coarsening, Muñoz-García and co-workers recently developed a new nonlinear model following a hydrodynamic approach [38]. In this approach, Muñoz-García *et al.* considered two coupled fields

$$\frac{\partial h}{\partial t} = -\Gamma_{ex} + \Gamma_{ad}, \tag{2.42}$$

$$\frac{\partial R}{\partial t} = (1-\phi)\Gamma_{ex} - \Gamma_{ad} + K\nabla^2 R, \tag{2.43}$$

where h and R represent the surface height function and the thickness of the mobile surface adatom layer, respectively. Here, $\bar{\phi} = (1-\phi)$ is the fraction of eroded adatoms that become mobile, Γ_{ex} is the curvature dependent erosion rate and Γ_{ad} is the rate of addition to the immobile bulk. Γ_{ad} is given by

$$\Gamma_{ad} = \gamma_0 \left[R - R_{eq} \left(1 - \gamma_{2x} \frac{\partial^2 h}{\partial x^2} - \gamma_{2y} \frac{\partial^2 h}{\partial y^2} \right) \right] , \qquad (2.44)$$

with the mean nucleation rate for a flat surface γ_0, the variation in the nucleation rate with the surface curvatures $\gamma_{2x,y}$, and the thickness of the layer of mobile atoms generated thermally without bombardment R_{eq}. Γ_{ex} follows from microscopic derivations [68],

$$\begin{aligned} \Gamma_{ex} &= \alpha_0 \left[1 + \alpha_{1x} \frac{\partial h}{\partial x} + \nabla \left(\underline{\alpha_2} \nabla h \right) + \frac{\partial}{\partial x} \nabla \left(\underline{\alpha_3} \nabla h \right) + \nabla \left(\underline{\alpha_4} \nabla \nabla^2 h \right) \right. \\ & \left. + \frac{\partial}{\partial x} h \nabla \left(\underline{\alpha_5} \nabla h \right) + \nabla h \left(\underline{\alpha_6} \nabla h \right) \right] . \qquad (2.45) \end{aligned}$$

The coefficients $\underline{\alpha_i}$ of equation (2.45) are 2×2 diagonal matrices, except $\underline{\alpha_4} = \begin{bmatrix} \alpha_{4xx} & \alpha_{4xy} \\ \alpha_{4yx} & \alpha_{4yy} \end{bmatrix}$. In the framework of Sigmund's theory of sputtering, these coefficients can be related to those of the general equation (2.33) so that $\alpha_0 = v_0$, $\alpha_{1x} = -\gamma / v_0$, $\alpha_{2x,y} = -\nu_{x,y} / v_0$, $\alpha_{3x,y} = -\Omega_{x,y} / v_0$, $\alpha_{4ij} = -D_{ij} / v_0$, $\alpha_{5x,y} = -\xi_{x,y} / v_0$, and $\alpha_{6x,y} = -\zeta_{x,y} / v_0$.

Equations (2.42)-(2.45) can be approximated by performing a multiple scale expansion with a subsequent adiabatic elimination of R. This results in an equation similar to the general continuum equation (2.33) but with additional *conserved* KPZ nonlinearities [38]:

$$\begin{aligned} \frac{\partial h}{\partial t} &= -v_0 + \gamma \frac{\partial h}{\partial x} + \sum_{i=x,y} \left\{ -\nu_i \frac{\partial^2 h}{\partial i^2} + \zeta_i^{(1)} \left(\frac{\partial h}{\partial i} \right)^2 + \Omega_i \frac{\partial^2}{\partial i^2} \frac{\partial}{\partial x} h \right. \\ & \left. + \xi_i \left(\frac{\partial h}{\partial x} \right) \left(\frac{\partial^2 h}{\partial i^2} \right) \right\} - \sum_{i,j=x,y} \left\{ \mathcal{K}_{ij} \frac{\partial^2}{\partial i^2} \frac{\partial^2}{\partial j^2} h + \zeta_{ij}^{(2)} \frac{\partial^2}{\partial i^2} \left(\frac{\partial h}{\partial j} \right)^2 \right\} . \qquad (2.46) \end{aligned}$$

The coefficients of the hydrodynamic model differ from those of the general equation and are given by [68]

$$\gamma = -\phi\alpha_0\alpha_{1x}, \tag{2.47}$$

$$\nu_x = \phi\alpha_0\alpha_{2x} - \frac{\alpha_0^2}{\gamma_0}\bar{\phi}\phi\alpha_{1x}^2, \tag{2.48}$$

$$\nu_y = \phi\alpha_0\alpha_{2y}, \tag{2.49}$$

$$\zeta_i^{(1)} = -\phi\alpha_0\alpha_{6i}, \tag{2.50}$$

$$\Omega_i = \alpha_0\left[-\phi\alpha_{3i}\left(\frac{\bar{\phi}K}{\gamma_0} - \phi R_{eq}\gamma_{2i}\right)\alpha_{1x}\right], \tag{2.51}$$

$$\xi_i = \phi\alpha_0\alpha_{5i}, \tag{2.52}$$

$$\mathcal{K}_{ij} = KR_{eq}\gamma_{2i} + \alpha_0\left[\phi\alpha_{4ij} - \left(\frac{K\bar{\phi}}{\gamma_0} - \phi R_{eq}\gamma_{2i}\right)\alpha_{2j}\right], \tag{2.53}$$

$$\zeta_{ij}^{(2)} = -\alpha_0\left(\frac{\bar{\phi}K}{\gamma_0} - \phi R_{eq}\gamma_{2i}\right)\alpha_{6j}. \tag{2.54}$$

The main novelty of the hydrodynamic model is the incorporation of *redeposition* of eroded material to the surface with the parameter ϕ controlling the amount of redeposited atoms. A key feature of the coupled two-field model is the presence of ripple coarsening which is probably induced by the conserved KPZ nonlinearity [38, 69]. Depending on the ratio between the coefficients of the conserved and the nonconserved KPZ terms, i.e. $\zeta_i^{(1)}$ and $\zeta_{ij}^{(2)}$, very different time dependencies of the ripple wavelength have been observed, ranging from marginal logarithmic to strong power-law coarsening. Moreover, in agreement with some experiments [8, 10, 11, 31], the observed coarsening is interrupted at certain times and the wavelength saturates at a constant value [38].

Chapter 3

Pattern Evolution in the Anisotropic Kuramoto-Sivashinsky Equation

Both the stochastic and the deterministic Kuramoto-Sivashinsky (KS) equation in one and two dimensions have been studied extensively during the last two decades, numerically as well as analytically. Most of these studies were either dedicated to investigate the scaling behavior of the surface in the asymptotic case [24, 26, 42, 70, 71], or focused on rather special phenomena of the surface evolution like the appearance of rotated ripple structures [25,72,73]. However, no detailed picture of the nonlinear surface evolution in the KS equation is provided yet, especially for the anisotropic case. In this chapter, numerical integrations of the anisotropic stochastic KS equation with and without damping are presented. For all the simulations, the spatial discretization introduced by Lam and Shin for the nonlinear terms [74] has been used with periodic boundary conditions. In the simulations, the influence of the strength of anisotropy and the applied damping on the surface morphology in the nonlinear regime has been investigated systematically.

3.1 The role of anisotropy: ripple rotation

Although most experimental studies on ion-induced pattern formation were performed under oblique ion incidence [52], only few theoretical studies [25, 72, 73] focused on the corresponding anisotropic KS (aKS) equation. These few studies showed that for long times, the initial ripple pattern vanishes and the surface enters kinetic roughening as in the isotropic case. For even longer times, however, the appearance of rotated ripple structures was observed under certain conditions [72].

In recent experiments on off-normal low-energy ion sputtering of Si(111) at high temperatures, i.e. in the presence of isotropic thermal diffusion, Brown and Erlebacher indeed observed a rotation of the initial ripple pattern with fluence [44, 53]. At low fluences, a periodic ripple pattern oriented normal to the direction of the incident ion beam formed on the surface. At intermediate fluences, however, another ripple pattern rotated by 90° overlayed the initial one, resulting in a tetragonal pattern of dot-like features. At even higher fluences, the initial pattern vanished and only the rotated pattern with a significantly larger wavelength remained.

Similar to these experimental observations, numerical integrations of the KS equation with and without noise showed the formation of new rotated ripples long after the initial pattern had vanished in the special case of $\zeta_x\zeta_y < 0$ [25, 72, 73]. These ripples represent one-dimensional solutions of equation (2.26) for which the nonlinearities precisely cancel and are, therefore, called *cancellation modes*. The angle of rotation is obtained by moving to a rotated coordinate system that cancels the nonlinear terms in the transverse direction and is given by $\phi_c = \tan^{-1}\sqrt{-\zeta_{x,y}/\zeta_{y,x}}$ [34, 72]. However, the experimentally observed rotation of the ripple pattern by 90° does not agree with the predicted angle of rotation which under these experimental conditions is expected to be $\phi_c \sim 25°$ [44]. Therefore, the observed ripple rotation is not related to the appearance of cancellation modes and must be of different origin. This stresses the importance of a systematic analysis of the surface evolution in the nonlinear regime of the aKS equation.

In order to study the influence of anisotropy on the surface morphology, it is convenient to transform equation (2.26) into a minimal equation. As a first step, by introducing a co-moving frame of reference, the erosion velocity of the flat surface v_0 is omitted. Then, the term $\gamma\partial h/\partial x$ which just causes a lateral drift of the pattern can be eliminated by the transformation $h(x, y, t) \rightarrow h(x - \gamma t, x, t)$. Under the assumption of isotropic diffusion, the aKS equation is then given by

$$\frac{\partial h}{\partial t} = \nu_x \frac{\partial^2 h}{\partial x^2} + \nu_y \frac{\partial^2 h}{\partial y^2} + \frac{\zeta_x}{2}\left(\frac{\partial h}{\partial x}\right)^2 + \frac{\zeta_y}{2}\left(\frac{\partial h}{\partial y}\right)^2 - K\nabla^4 h + \eta. \tag{3.1}$$

Finally, rescaling the time by $(\nu_x^2/K)t \rightarrow t$, the lateral scales by $\sqrt{|\nu_x|/K}\mathbf{x} \rightarrow \mathbf{x}$, the height by $-(\zeta_x/2\nu_x)h \rightarrow h$, and the noise by $-(\zeta_x K/2\nu_x^3)\eta \rightarrow \eta$ leads to the minimal equation

$$\frac{\partial h}{\partial t} = -\frac{\partial^2 h}{\partial x^2} - a_\nu \frac{\partial^2 h}{\partial y^2} + \left(\frac{\partial h}{\partial x}\right)^2 + a_\zeta\left(\frac{\partial h}{\partial y}\right)^2 - \nabla^4 h + \eta \tag{3.2}$$

with the new coefficients $a_\nu = \nu_y/\nu_x$ and $a_\zeta = \zeta_y/\zeta_x$. These two coefficients a_ν and a_ζ control the strength of the linear and the nonlinear anisotropy, respectively.

The numerical integration of equation (3.2) was performed on a grid with 200 × 200 lateral nodes with $\Delta x = \Delta y = 1$. The integration step was $\Delta t = 0.01$ and the noise amplitude was fixed at $D_\eta = 0.01$.

Fig. 3.1 shows the simulated morphologies for constant $a_\nu = 0.1$ and different values of a_ζ at three different times. At short times (left column), a periodic ripple pattern forms for all three a_ζ values. The amplitude of the ripples grows exponentially until the surface enters the nonlinear regime and undergoes kinetic roughening. Here, the initial ripple patterns vanish. For $a_\zeta = 0.5$, the resulting stationary morphology in this regime is rather isotropic (see Fig. 3.1(b,c)). For a lower a_ζ value of 0.1, however, the stationary morphology exhibits a significant anisotropy (see Fig. 3.1(e,f)). Lowering a_ζ even further to 0.0001, one observes a similar anisotropic morphology at $t = 200$ (Fig. 3.1(h)). At $t = 1000$, however, this anisotropic morphology has developed a periodicity and a new ripple pattern with larger wavelength now dominates the surface morphology. This pattern is rotated by 90° with respect to the initial pattern.

In these simulations, $a_\zeta = \zeta_y/\zeta_x$ was always positive. Therefore, the observed rotated ripple patterns cannot be explained by cancellation modes. In addition, they appear only for a rather strong nonlinear anisotropy $a_\zeta \ll 1$. This can be interpreted in the following way [75]. In the asymptotic case of long times, it has been shown that the one-dimensional KS equation renormalizes to the one-dimensional KPZ equation with a positive linear coefficient ν^* [42]. Then, the surface instability is lost and the morphology undergoes kinetic roughening. The same is assumed for the two-dimensional isotropic KS equation [42]. In the case of the aKS equation with a_ζ close to zero, one can expect that this renormalization is still valid in the x-direction, resulting in a positive ν_x^*. In the y-direction, however, the nonlinearity is so weak that the transition to the nonlinear regime is strongly delayed (cf. equation (2.30)). Therefore, at the time when the x-direction is already renormalized to a $\nu_x^* > 0$, the y-direction does not yet renormalize and $\nu_y^* = \nu_y$ remains negative. Then, $a_\nu^* = \nu_y^*/\nu_x^* < 0$ leads to a new linear instability in the y-direction that causes the formation of another ripple pattern rotated by 90°. These ripples then grow exponentially in time until also the y-direction renormalizes and the ripple amplitude saturates. According to equation (2.30), the time t_{c2} of this saturation should follow the

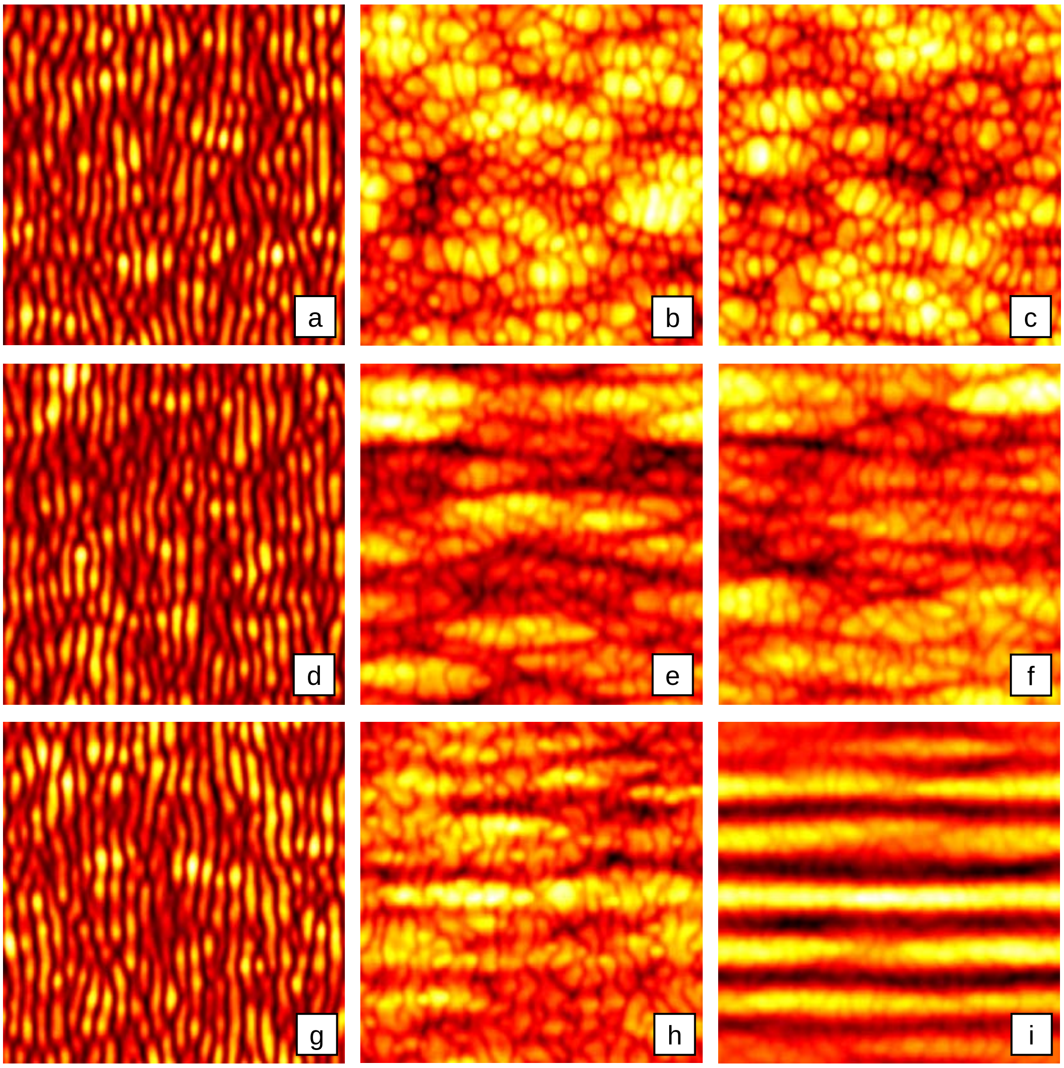

Figure 3.1: Morphology for $a_\nu = 0.1$ and $a_\zeta = 0.5$ (first row), $a_\zeta = 0.1$ (second row), and $a_\zeta = 0.0001$ (third row) at $t = 20$ (left), 200 (center), and 1000 (right).

relation

$$t_{c2} \propto \frac{1}{a_\nu^2} \ln\left(\frac{a_\nu}{a_\zeta}\right). \tag{3.3}$$

Therefore, t_{c2} should scale both with a_ν and a_ζ. In addition, the wavelength of the rotated

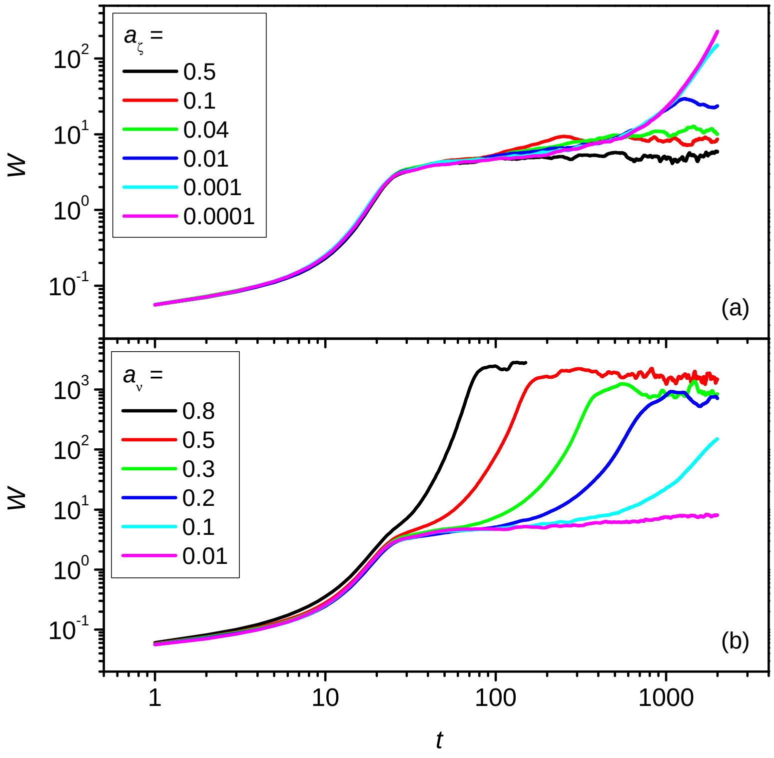

Figure 3.2: Evolution of the global two-dimensional interface width W for (a) different values of a_ζ with $a_\nu = 0.1$ and (b) different values of a_ν with $a_\zeta = 0.001$. All units are arbitrary.

pattern should follow from equation (2.25),

$$\lambda_y = 2\pi\sqrt{\frac{2}{a_\nu}}. \tag{3.4}$$

Fig. 3.2(a) depicts the evolution of the global two-dimensional interface width W (see chapter 4.1, equation (4.1)) for different values of a_ζ at constant a_ν. As soon as the initial ripple pattern has formed, the ripple amplitude and, therefore, also W grows exponentially with time. When entering the kinetic roughening regime at t_{c1}, W saturates. For a rather large a_ζ of 0.5, W remains rather constant after this saturation. For $a_\zeta = 0.1$, however, a short exponential increase can be observed for $t \gtrsim 100$, indicating the formation and growth of the rotated pattern. At $t_{c2} \approx 200$, however, the growth is interrupted and W

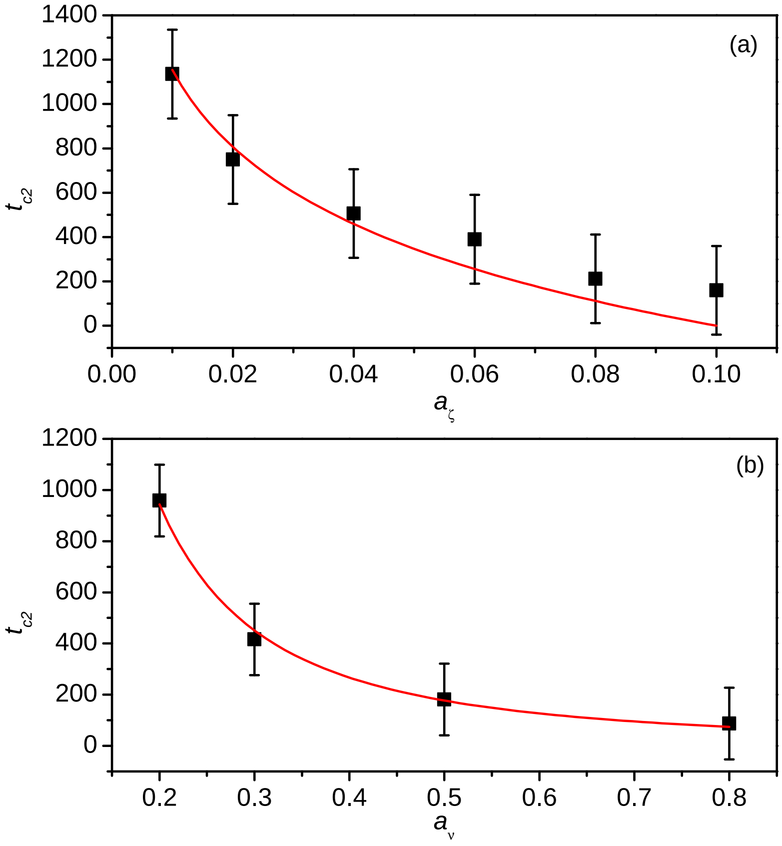

Figure 3.3: Transition time t_{c2} vs. (a) a_ζ for $a_\nu = 0.1$ and (b) a_ν for $a_\zeta = 0.001$. The solid lines represent fits according to equation (3.3) with a prefactor as the fitting parameter. All units are arbitrary.

saturates at a slightly higher value. With decreasing a_ζ, this saturation is further delayed as t_{c2} increases. A similar behavior is observed for the dependence of W on a_ν given in Fig. 3.2(b) with t_{c2} increasing with decreasing a_ν. Both these dependencies agree qualitatively with the expected behavior of t_{c2} from equation (3.3). In addition, also the growth of the amplitude of the rotated ripples is affected by a_ν. This can be interpreted as resulting from the ν_y dependence of the growth factor $R_{k_y^*} = f(\nu_y)$ (cf. equation (2.23)).

A quantitative comparison between the simulated and the analytical dependence of t_{c2} on a_ζ and a_ν is shown in Fig. 3.3(a) and (b), respectively. Here, the square symbols give

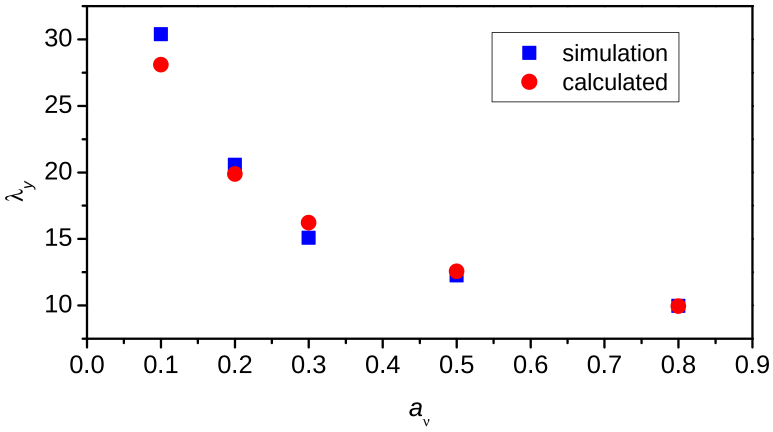

Figure 3.4: Wavelength λ_y of the rotated pattern vs. a_ν determined from the simulations for $a_\zeta = 0.001$ (squares) and calculated using equation (3.4) (circles). The error bars are smaller than the symbol size. All units are arbitrary.

the value of t_{c2} as determined from the simulations and the solid lines represent fits of the data according to equation (3.3). In both cases, the simulated t_{c2} values are in good agreement with the analytical prediction of equation (3.3). A comparison between the wavelength λ_y of the rotated ripple pattern in dependence of a_ν and the corresponding λ_y values as calculated from equation (3.4) is given in Fig. 3.4. Again, both data sets agree fairly well.

The here presented data supports the above assumption that the observed rotated ripple pattern actually results from the fact that the renormalization of the aKS equation occurs earlier in the x than in the y-direction. However, in order to confirm this hypothesis, analytical evidence is needed.

Comparison of the above simulations with the experimental results of Brown *et al.* reveals striking similarities [44, 53] like the observed 90° rotation and the larger wavelength of the rotated patterns. Therefore, a strong nonlinear anisotropy with $a_\zeta \ll 1$ can be assumed for the experimental system investigated in references [44] and [53]. Also transient morphologies of two-dimensional features similar to those observed in the experiments can be achieved in the simulations of the aKS equation by tuning the a_ν and a_ζ coefficients

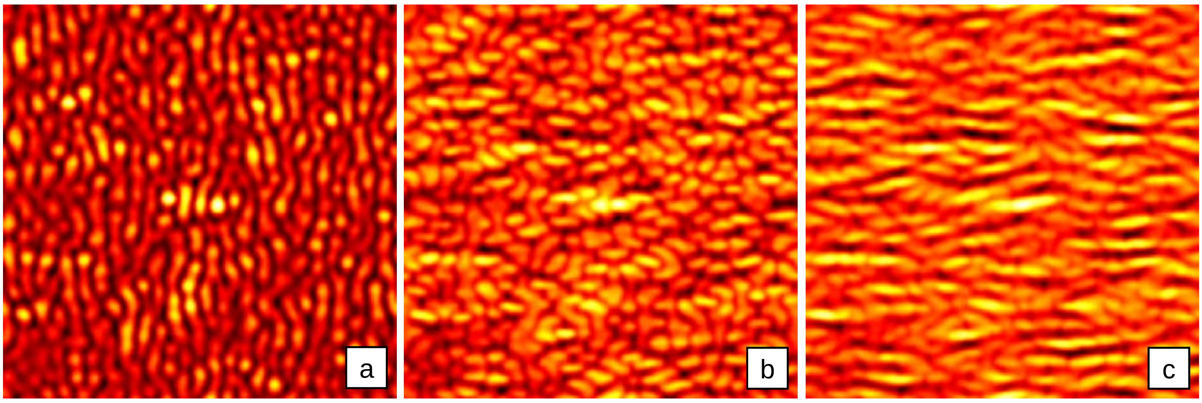

Figure 3.5: Morphology transition with intermediate two-dimensional features obtained for $a_\nu = 0.7$ and $a_\zeta = 0.001$ at $t = 17$ (a), 27 (b), and 37 (c).

in a way, that the growth of the rotated ripples sets in before the initial pattern has fully vanished. Such a transition is shown in Fig. 3.5 for $a_\nu = 0.7$ and $a_\zeta = 0.001$.

One experimental finding that cannot be explained by the here presented simulations is the coarsening of both the initial and the rotated ripple pattern as observed by Brown *et al.* [44, 53]. Wavelength coarsening is generally considered as a truly nonlinear feature. However, in the aKS simulations, the initial ripple pattern forms in the linear regime and gets destroyed when the ζ_x nonlinearity becomes active. Therefore, no coarsening of the initial pattern can be expected. The rotated pattern also forms in a linear regime without the possibility of wavelength coarsening. When also the ζ_y nonlinearity becomes active, the ripple amplitude saturates but the rotated pattern does not immediately get destroyed by kinetic roughening. However, no coarsening of the remaining pattern has been observed.

3.2 The role of damping: ripple coarsening

The isotropic KS equation with damping could successfully explain the experimentally observed formation of hexagonally ordered dot patterns under normal incidence ion sputtering [9,35,63,66]. However, the isotropic dKS equation failed to reproduce the coarsening of the dot periodicity as observed in some experiments [10, 11, 65].

The anisotropic dKS (adKS) equation (2.32) has been studied less intensively and mainly for rather special cases like structuring with multiple ion beams [65] or to explain the experimentally observed transition from ripple to dot patterns [64]. In this section, a detailed study of the adKS equation is presented with special emphasis on the role of the applied damping. In contrast to the isotropic case, moderate ripple coarsening is observed in a certain parameter range.

In order to reduce the number of simulation parameters, equation (2.32) has been transformed to a minimal equation by applying the same procedure as described in the previous section. The resulting minimal equation is given by

$$\frac{\partial h}{\partial t} = -a_\kappa h - \frac{\partial^2 h}{\partial x^2} - a_\nu \frac{\partial^2 h}{\partial y^2} + \left(\frac{\partial h}{\partial x}\right)^2 + a_\zeta \left(\frac{\partial h}{\partial y}\right)^2 - \nabla^4 h + \eta \tag{3.5}$$

with a_ν and a_ζ as defined in equation (3.1) and $a_\kappa = (K/\nu_x^2)\kappa$.

Equation (3.5) has been numerically integrated on a grid consisting of 300×300 lateral nodes with $\Delta x = \Delta y = 1$ and $\Delta t = 0.01$. The noise amplitude was $D_\eta = 0.01$. To study the influence on the damping on the surface morphology, $a_\nu = 0.1$ and $a_\zeta = -1$ have been used in the simulations. For these parameters, the growth rate of the ripple amplitude is $R_{k_c} = 0.25$. Therefore, for $a_\kappa > 0.25$, the effective growth rate $R^*_{k_c} = R_{k_c} - a_\kappa$ becomes negative and ripple formation is suppressed.

The surface morphology at three different stages of the evolution is shown in Fig. 3.6 for $a_\kappa = 0$ (first row), 0.10 (second row), and 0.20 (third row). One can clearly see the influence of the damping term on the pattern evolution. In the beginning, ordered ripple patterns form for all three values of a_κ but with different amplitude (Fig. 3.6, left column). At $t = 50$, however, the pattern has already vanished for $a_\kappa = 0$ (Fig. 3.6(b)), whereas ripple patterns of different quality are still visible for $a_\kappa = 0.10$ and 0.20 (Fig. 3.6(e,h)). With increasing time, the quality of these ripple patterns decreases and increases for $a_\kappa = 0.10$ and 0.20, respectively, until a steady state is reached (see Fig. 3.6(f,i)). At the same time, the periodicity of the ripples is slightly increasing for $a_\kappa = 0.10$ whereas it remains rather constant for $a_\kappa = 0.20$. In the case of $a_\kappa = 0$, no steady state is observed and the surface roughens continuously. For long integration times (Fig. 3.6(c)), one can even observe the formation of cancellation modes in the undamped equation.

The two-dimensional global interface width W has been calculated from the simulated morphologies and is shown in Fig. 3.7. For $a_\kappa = 0$, W grows exponentially with time until a transition to a power law growth occurs when the surface enters the nonlinear regime at $t_c \sim 25$. For $a_\kappa \neq 0$, this power law growth is suppressed and W saturates when

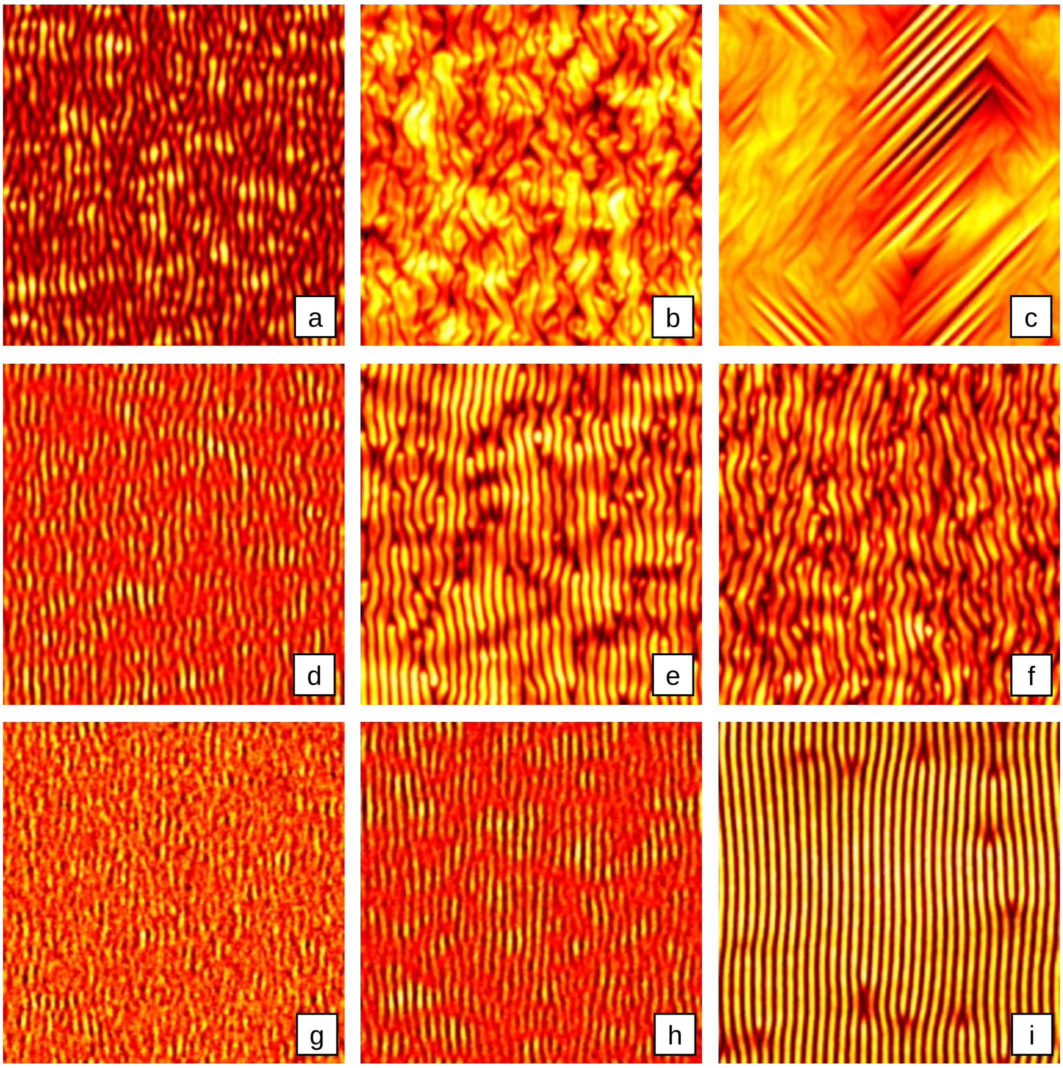

Figure 3.6: Morphology for $a_\nu = 0.1$, $a_\zeta = -1$, and $a_\kappa = 0$ (first row), 0.10 (second row), and 0.20 (third row) at $t = 20$ (left), 50 (center), and 500 (right).

entering the nonlinear regime at t_c. With increasing a_κ, t_c is shifted to later times and the saturation value of the interface width decreases.

The evolution of the ripple patterns has been studied by evaluating the one-dimensional power spectral density or structure factor $S_x(k_x)$ (see chapter 4.1, equation (4.6)) in the x direction, i.e. across the ripples. Fig. 3.8 shows $S_x(k_x)$ calculated at dif-

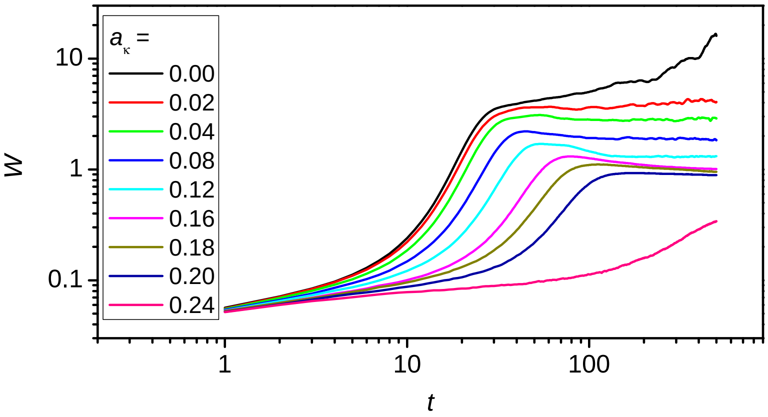

Figure 3.7: Evolution of $W(t)$ for $a_\nu = 0.1$, $a_\zeta = -1$ and different values of a_κ. All units are arbitrary.

ferent times from the simulated morphologies for $a_\kappa = 0$ (Fig. 3.8(a)), 0.10 (Fig. 3.8(b)), and 0.20 (Fig. 3.8(c)), respectively. In the linear regime at $t = 10$, for all three values of a_κ the $S_x(k_x)$ curves exhibit a BH-like peak that corresponds to the wavelength λ of the formed ripple pattern and grows exponentially with time. In the nonlinear regime, however, certain differences can be observed. For $a_\kappa = 0$ (Fig. 3.8(a)), the peak decays rather fast until it has completely vanished already at $t = 60$. During this decay, the peak shape is changing and the peak maximum shifts slightly to lower k_x values. On the contrary, for $\kappa = 0.20$ (Fig. 3.8(c)), the peak gets narrower and higher order peaks appear, indicating an increased ordering of the ripples. Here, the peak position is constant in time. For intermediate a_κ values as shown in Fig. 3.8(b), however, the peak position is slightly shifting to lower k_n values until a steady state is reached at long times.

Fig. 3.9 gives the ripple wavelength λ as a function of time for the different a_κ values. The wavelength for the different morphologies was determined from the position of the local maximum of the structure factor curves. In the linear regime, λ remains constant for all values of a_κ. When entering the nonlinear regime at t_c, a rapid increase of λ is observed for $a_\kappa = 0$ shortly before the periodic ripple structure is lost due to kinetic roughening. However, in Fig. 3.6(b), one can see that the resulting surface is not randomly

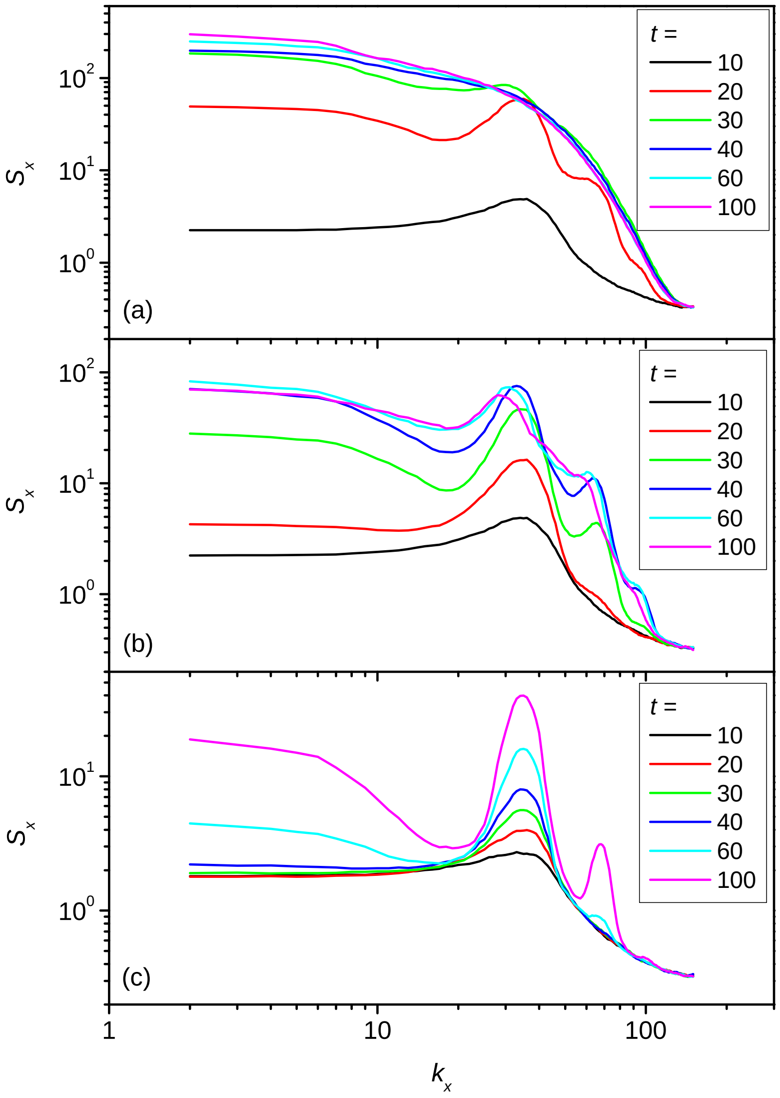

Figure 3.8: Structure factors $S_x(k_x)$ in x direction at six different times for $a_\kappa = 0$ (a), 0.10 (b), and 0.20 (c). All units are arbitrary.

rough but still exhibits anisotropic structures, the remains of the ripple pattern. The characteristic length of these structures is significantly larger than the ripple wavelength which indicates that coarsening is also present in the undamped case but masked by

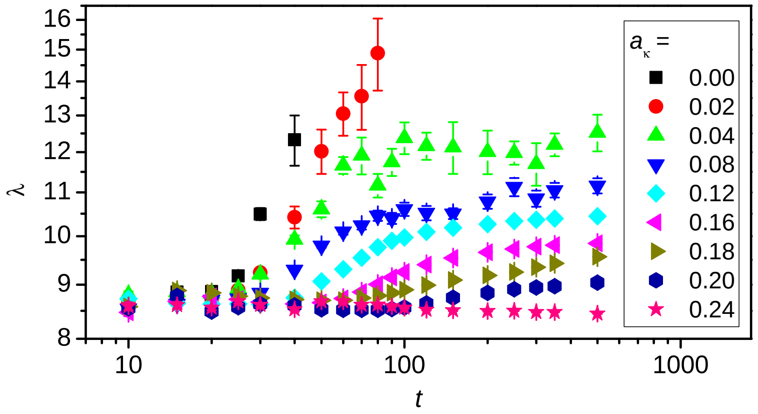

Figure 3.9: Evolution of λ for different values of a_κ with $a_\nu = 0.1$ and $a_\zeta = -1$. All units are arbitrary.

the kinetic roughening of the surface. With increasing a_κ, the ripple pattern is getting stabilized in the nonlinear regime and the transition to kinetic roughening occurs later. For $a_\kappa = 0.04$, the morphology enters a steady state at $t \sim 100$ with a remaining ripple pattern of constant periodicity. A further increase of a_κ leads to a decrease of the saturation value of λ. For $a_\kappa \geq 0.20$, nearly no coarsening occurs and λ remains approximately constant for all times.

Fig. 3.10 shows the exponents of ripple coarsening n for the different a_κ values as determined from power law fits of the wavelength data in the coarsening regime. With increasing a_κ, the coarsening exponent decreases from $n \sim 0.47$ at $\kappa = 0.02$ to $n \sim 0$ at $\kappa \geq 0.24$. With few exceptions [32], this range covers the coarsening exponents observed in most experimental studies (cf. e.g. references [29, 30, 33, 76]).

Since no wavelength coarsening has ever been observed in simulations of the well studied isotropic dKS equation [35, 62, 63, 66], an anisotropy effect appears to be a likely explanation for the ripple coarsening found in the current simulations. In order to verify this assumption, the strength of the linear and the nonlinear anisotropy has been varied at constant damping $a_\kappa = 0.04$. The linear anisotropy parameter a_ν was found to have no influence on the coarsening of the ripples. The nonlinear anisotropy parameter a_ζ, however, strongly affects to evolution of the ripple wavelength as can be seen in Fig. 3.11.

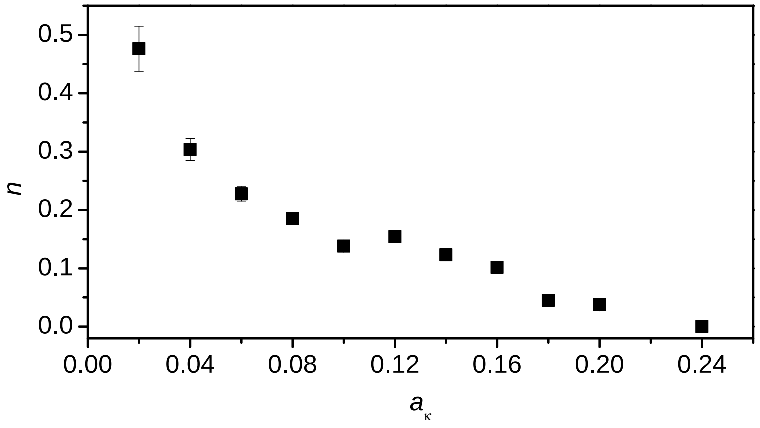

Figure 3.10: Coarsening exponent n as function of a_κ for $a_\nu = 0.1$ and $a_\zeta = -1$. All units are arbitrary.

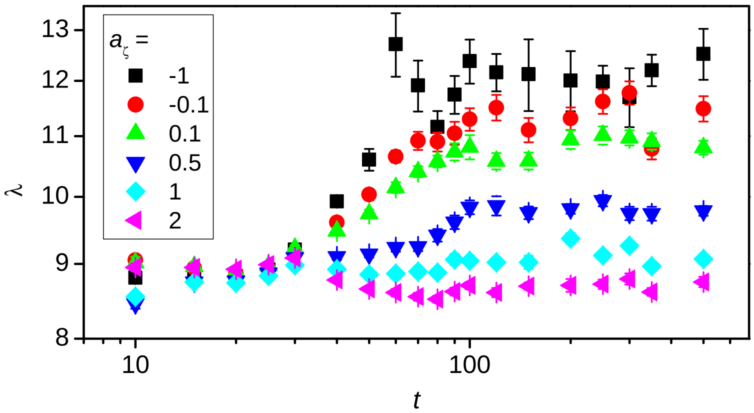

Figure 3.11: Evolution of λ for $a_\kappa = 0.04$, $a_\nu = 0.1$, and different values of a_ζ. All units are arbitrary.

The strongest coarsening is observed for $a_\zeta = -1$. For $a_\zeta < -1$, cancellation modes superpose the ripple pattern so that the wavelength cannot be determined reliably. With increasing a_ζ, however, the coarsening gets weaker and the final wavelength decreases. At $a_\zeta = 1$, nearly no coarsening is observed anymore and the wavelength remains rather constant.

This a_ζ dependence indicates that the observed coarsening in the adKS equation indeed results from a purely nonlinear anisotropy effect which accounts for the absence of dot coarsening in the isotropic case, i.e. $a_\nu = a_\zeta = 1$. In addition, the fact that no coarsening has been observed in the few previous adKS studies [64,65] can be explained by the narrow range $-1 \leq a_\zeta < 1$ in which ripple coarsening takes place.

Compared to the hydrodynamic model developed by Muñoz-García and coworkers [38], the ripple coarsening in the adKS equation is a rather small effect. In the hydrodynamic model, the ripple wavelength was found to increase up to a factor of about 6 [69], whereas in the present simulations the increase of the wavelength was only about 70% at maximum (cf. Fig. 3.9). Nevertheless, the numerical work presented here demonstrates the applicability of the anisotropic dKS equation to ion erosion systems in the presence of ripple coarsening. However, in order to understand the origin of ripple coarsening in this equation, further analytical studies of the adKS equation are needed. In addition, because of the strong influence of the damping coefficient κ on the coarsening behavior, the correct determination of κ for an experimental system remains a crucial task. Therefore, a comprehensive understanding of the physical origin of the damping term in ion erosion is necessary.

Chapter 4

Dynamic Scaling Theory

Because of the high demand for surfaces with tailored physical properties for various technological applications, much effort has been spent on the investigation and quantitative description of different (positive and negative) surface growth processes [39,77,78]. In many cases, the surface morphology was found to exhibit spatial and temporal fluctuations which obey scaling relations similar to those of equilibrium critical phenomena [40,41]. As in the case of these phenomena, scaling exponents can be determined which characterize the fluctuations of the surface and do *not* depend on microscopic details of the system under investigation. Based on these scaling exponents, a particular growing surface can be assigned to a certain universality class and, therefore, to a certain continuum model that is able to describe the system under investigation [39]. In the following, the relevant scaling concepts of rough surfaces will be briefly summarized.

4.1 Dynamic scaling concepts

A growing surface is characterized in space and time by its so-called *global* interface width

$$W(L,t) = \left\langle \left\langle \left[h\left(\mathbf{r},t\right) - \bar{h}(t) \right]^2 \right\rangle_L^{1/2} \right\rangle_\eta \tag{4.1}$$

which describes the fluctuations of surface heights around the mean height $\bar{h}(t) = \langle h(\mathbf{r},t)\rangle_L$. Here, $\langle ... \rangle_L$ denotes spatial averaging over the whole system of size L and $\langle ... \rangle_\eta$ denotes averaging over different realizations of the noise which in the case of experimental systems corresponds e.g. to an average over different identically processed samples.

In many growth processes, the global interface width is observed to satisfy the dynamic scaling *Ansatz* of Family and Vicsek (FV) [39, 79],

$$W(L,t) = t^{\alpha/z} f\left(L/t^{1/z}\right) \tag{4.2}$$

with the roughness exponent α, the dynamic exponent z, and the scaling function

$$f(u) \propto \begin{cases} \text{const.} & \text{if} \quad u \gg 1, \\ u^{\alpha} & \text{if} \quad u \ll 1. \end{cases} \tag{4.3}$$

For long times $t \gg L^z$, the surface enters a stationary regime in which the correlation length $\xi(t) \propto t^{1/z}$ has exceeded the system size L. Then, the surface morphology is characterized by the roughness exponent α. In the limit of short times $t \ll L^z$, the behavior of the surface is characterized by the so-called growth exponent $\beta = \alpha/z$.

For experimental systems, the global interface width is usually not accessible because of the large system sizes that can easily exceed the centimeter range. Therefore, the so-called *local* interface width

$$w(l,t) = \left\langle \left\langle \left[h\left(\mathbf{r},t\right) - \bar{h}(t)\right]^2 \right\rangle_l^{1/2} \right\rangle_\eta \tag{4.4}$$

calculated over an observation window of size $l \ll L$ is often used to evaluate the dynamics of a rough surface. In the presence of FV dynamic scaling as in equation (4.2), the local interface width of a self-affine surface, i.e. a surface without any characteristic length scale besides the system size, should exhibit the same scaling behavior as the global interface width [80]. Then, at small length scales $l \ll \xi$, $w(l,t) \propto l^{\alpha}$. At long distances $l \gg \xi$, the local width scales with time as $w(l,t) \propto t^{\beta}$. For non-self-affine surfaces, however, the local and the global interface width may exhibit different scaling behaviors [80, 81].

In experimental as well as theoretical studies, the so-called height-height correlation function is frequently used to investigate the dynamic scaling behavior of growing surfaces. The height-height correlation function is defined as

$$C(\mathbf{l},t) = \left\langle \left\langle \left[h(\mathbf{l}+\mathbf{r},t) - h(\mathbf{r},t)\right]^2 \right\rangle_L \right\rangle_\eta \tag{4.5}$$

and scales as the square of the local interface width, $C(l,t) \propto w^2(l,t)$. Alternatively, the scaling behavior of a surface can also be studied in momentum space by evaluating its power spectral density or structure factor which is related to the height-height correlation function as

$$S(\mathbf{k},t) = \left\langle \tilde{h}(\mathbf{k},t)\tilde{h}(-\mathbf{k},t) \right\rangle_\eta = \frac{1}{2}\sum_{\mathbf{l}} \left(\delta(\mathbf{k}-\mathbf{0}) - e^{i\mathbf{k}\mathbf{l}}\right) C(\mathbf{l},t) \tag{4.6}$$

with the Fourier transform of the surface height $\tilde{h}(\mathbf{k}, t)$ and the spatial frequency $\mathbf{k}$. In the case of FV scaling, the structure factor can be expressed by the relation [39]

$$S(k, t) = k^{-(2\alpha+d)} s(kt^{1/z}), \tag{4.7}$$

with

$$s(u) \propto \begin{cases} \text{const.} & \text{if} \quad u \gg 1, \\ u^{2\alpha+d} & \text{if} \quad u \ll 1. \end{cases} \tag{4.8}$$

Here, d represents the dimensionality of the surface which is e.g. $d = 2$ if S was calculated from a two-dimensional surface and $d = 1$ if S was calculated from a one-dimensional surface or one-dimensional cuts of a two-dimensional surface. Compared to equation (4.2), the structure factor has the advantage that only the long wavelength modes contribute to its scaling what minimizes the influence of finite-size effects or sampling related artifacts [39].

4.2 An example: the Edwards-Wilkinson equation

In general, the dynamic scaling exponents of a continuum equation can be determined under the assumption of self-affinity by rescaling the equation in space and time. For nonlinear equations like the KS equation that cannot be solved in closed form, however, one usually has to use approximation methods like the dynamic renormalization group approach [42]. Therefore, in this section, the analytic determination of the dynamic scaling exponents shall be demonstrated by the example of the linear Edwards-Wilkinson (EW) equation [39].

The EW equation was the first continuum equation used to study the growth of surfaces by particle deposition. It only consists of a linear and a noise term and has the form [39]

$$\frac{\partial h(\mathbf{x}, t)}{\partial t} = \nu \nabla^2 h(\mathbf{x}, t) + \eta(\mathbf{x}, t). \tag{4.9}$$

If the surface described by this equation is self-affine, then rescaling it both laterally and vertically by $\mathbf{x} \rightarrow \mathbf{x}' \equiv b\mathbf{x}$ and $h \rightarrow h' \equiv b^{\alpha} h$, respectively, should result in a surface that is statistically indistinguishable from the original one [39]. In addition, since the interface width also depends on the time, the time has to be rescaled by $t \rightarrow t' \equiv b^z t$.

The delta-correlated noise term in equation (4.9) is defined by

$$\langle \eta(\mathbf{x}, t) \eta(\mathbf{x}', t') \rangle = 2D_{\eta} \delta^d(\mathbf{x} - \mathbf{x}') \delta(t - t'). \tag{4.10}$$

Rescaling this relation results in

$$\langle \eta(b\mathbf{x}, b^z t)\eta(b\mathbf{x}', b^z t')\rangle = 2D_\eta \delta^d(b\mathbf{x} - b\mathbf{x}')\delta(b^z t - b^z t'). \tag{4.11}$$

By using the property of the delta function $\delta^d(a\mathbf{x}) = a^{-d}\delta^d(\mathbf{x})$, one obtains

$$\langle \eta(b\mathbf{x}, b^z t)\eta(b\mathbf{x}', b^z t')\rangle = 2D_\eta b^{-(d+z)}\delta^d(\mathbf{x} - \mathbf{x}')\delta(t - t'). \tag{4.12}$$

Therefore, by rescaling equation (4.9) one finds

$$b^{\alpha-z}\frac{\partial h}{\partial t} = \nu b^{\alpha-2}\nabla^2 h + b^{-(d+z)/2}\eta. \tag{4.13}$$

Multiplying both sides of equation (4.13) by $b^{z-\alpha}$ leads to

$$\frac{\partial h}{\partial t} = \nu b^{z-2}\nabla^2 h + b^{-d/2+z/2-\alpha}\eta. \tag{4.14}$$

In order to ensure the scale invariance of the EW equation, each term on the right-hand side of equation (4.14) must be independent of b. Therefore, $\alpha = (2-d)/2$, $z = 2$, and $\beta = \alpha/z = (2-d)/4$. Note that these results are valid for the EW equation in arbitrary dimensions d.

4.3 The dynamic scaling behavior of the KS equation

A growing surface that is described by a more complex continuum equation like the KS equation might exhibit not only one but several spatial and temporal regimes which are governed by the individual terms present in the corresponding equation. In these regimes, the surface roughness will thus exhibit a certain spatiotemporal behavior that is characteristic for the contributing terms. Therefore, by analyzing the dynamic scaling behavior of a growing surface in space and time, one can gain information about the contributing linear and nonlinear terms in the corresponding continuum equation.

In numerical integrations of the KS equation in $1+1$ dimensions, Cuerno and co-workers have identified the signatures of the contributing terms from the evolution of the global interface width W [26]. At very short times, W was found to grow with an exponent $\beta_\eta = 0.5$ corresponding to random erosion dominated by the noise term η. Then, a crossover to $\beta_{MBE} = 0.38$ was observed which is the growth exponent of the linear molecular beam epitaxy (MBE) equation in $1+1$ dimensions,

$$\frac{\partial h}{\partial t} = -K\frac{\partial^4 h}{\partial x^4} + \eta. \tag{4.15}$$

Table 4.1: Dynamic scaling exponents of the different universality classes contributing to the evolution of the KS equation in $1+1$ dimensions.

Name	Equation	α	β	z	Reference
Random deposition/erosion	$\partial_t h = \eta$		1/2		[39]
Linear MBE	$\partial_t h = -\partial_x^4 h + \eta$	3/2	3/8	4	[80]
Edwards-Wilkinson	$\partial_t h = \partial_x^2 h + \eta$	1/2	1/4	2	section 4.2
Kardar-Parisi-Zhang	$\partial_t h = \partial_x^2 h + \lvert\partial_x h\rvert^2 + \eta$	1/2	1/3	3/2	[58]

Thus, in this regime, the surface morphology is governed by the surface diffusion term. The linear MBE growth is followed by a regime that is dominated by the BH instability resulting in the exponential growth of the interface width. Then, a transition to EW scaling occurs with $\beta_{EW} = 0.25$. Finally, in the nonlinear regime, the $1+1$ dimensional KS equation renormalizes to the KPZ equation and W grows with $\beta_{KPZ} = 1/3$ [26, 42]. The scaling exponents of the relevant universality classes that contribute to the dynamical evolution of the KS equation in $1+1$ and $2+1$ dimensions are summarized in table 4.1 and 4.2, respectively.

In addition to this complex dynamical behavior, depending on the initial parameters and boundary conditions, the system might get attracted to different so-called fixed points that determine different asymptotic states. Therefore, for different experimental parameters, the surface might exhibit different sets of scaling exponents in the asymptotic state corresponding to different fixed points. For example, the anisotropic KPZ equation (2.31)

Table 4.2: Dynamic scaling exponents of the different universality classes contributing to the evolution of the isotropic KS equation in $2+1$ dimensions.

Name	Equation	α	β	z	Reference
Random deposition/erosion	$\partial_t h = \eta$		1/2		[39]
Linear MBE	$\partial_t h = -\nabla^4 h + \eta$	1	1/4	4	[39]
Edwards-Wilkinson	$\partial_t h = \nabla^2 h + \eta$	0	0	2	section 4.2
Kardar-Parisi-Zhang	$\partial_t h = \nabla^2 h + \lvert\nabla h\rvert^2 + \eta$	0.38	0.24	1.6	[39]

is known to have two different fixed points [24]. For $\zeta_x\zeta_y > 0$, the asymptotic scaling behavior is characterized by a nonlinear isotropic KPZ fixed point whereas $\zeta_x\zeta_y < 0$ leads to logarithmic EW scaling. Moreover, also the system's approach towards the asymptotic state may depend on the boundary conditions, resulting in different transient scaling exponents. Thus, it is rather difficult to determine (all) the correct dynamic scaling exponents of a given system, especially for an experimental one.

4.4 Scaling of anisotropic surfaces

Anisotropic surfaces may exhibit an even more complex dynamic scaling behavior than isotropic ones since the anisotropy of the surface is reflected in the correlation function (4.5) [82–84]. Therefore, different roughness exponents $\alpha_{x,y}$ can be expected for correlations measured in the x and the y direction, respectively. Rescaling along the x direction in the stationary state, i.e. when neglecting any time dependence, then leads to [83]

$$C(x,y) \propto b^{\alpha_x} C(b^{-1}x, b^{-\chi_x}y) \tag{4.16}$$

with the anisotropy exponent $\chi_x = \alpha_x/\alpha_y$ accounting for the different rescaling factors along the two directions. Equivalently, rescaling along the y direction will result in

$$C(x,y) \propto b^{\alpha_y} C(b^{-\chi_y}x, b^{-1}y) \tag{4.17}$$

with $\chi_y = 1/\chi_x = \alpha_y/\alpha_x$. Thus, the scaling behavior of the anisotropic surface in *real space* is determined by the two independent exponents α_x and α_y.

In *momentum space*, however, similar definitions can be applied to the scaling of the structure factors of one-dimensional cuts along the x and the y direction what then leads to [84]

$$\begin{aligned} S(k_x) &\propto k_x^{-(2\tilde{\alpha}_x+2-\chi_x)}, \quad (4.18)\\ S(k_y) &\propto k_y^{-(2\tilde{\alpha}_y+2-\chi_y)} \quad (4.19) \end{aligned}$$

with the two independent roughness exponents in momentum space $\tilde{\alpha}_{x,y}$. Then, the relation between the roughness exponents in momentum and in real space is given by [84]

$$\begin{aligned} \tilde{\alpha}_x &= \alpha_x - \frac{1-\chi_x}{2} = \alpha_x - \frac{1-\alpha_x/\alpha_y}{2} \quad (4.20)\\ \tilde{\alpha}_y &= \alpha_y - \frac{1-\chi_y}{2} = \alpha_y - \frac{1-\alpha_y/\alpha_x}{2}. \quad (4.21) \end{aligned}$$

Therefore, the dynamic scaling behavior of the surface is described by *four different* roughness exponents that characterize the surface along the x or the y direction in momentum or real space. Only in the case of $\chi_x = \chi_y = 1$, i.e. isotropic scaling in real space with $\alpha_x = \alpha_y$, $\tilde{\alpha}_x = \alpha_x$ and $\tilde{\alpha}_y = \alpha_y$.

Equations (4.16) - (4.21) imply that the roughness exponents in momentum space can be calculated from the real space exponents determined from real space measurements. However, substituting equations (4.20) and (4.21) into equations (4.18) and (4.19) leads to

$$S(k_x) \propto k_x^{-(2\alpha_x+1)}, \tag{4.22}$$

$$S(k_y) \propto k_y^{-(2\alpha_y+1)}. \tag{4.23}$$

Therefore, in the case of $k_{x,y}t^{1/z} \gg 1$, the real space exponents can be determined from momentum space measurements by evaluating the one-dimensional structure factors in the x and the y directions, respectively.

Chapter 5

Experimental Techniques

In the experiments of this work, commercially available epi-polished Si(100) wafers with a native surface oxide have been bombarded with sub-keV Ar^+ ions. The sample surfaces have been characterized *ex-situ* (chapters 6.1 and 6.2) and *in-situ* (chapter 6.3) by atomic force microscopy and grazing incidence small angle X-ray scattering (GISAXS), respectively. The ion beam was extracted from a Kaufman type ion source mounted in a vacuum chamber with a base pressure of $\sim 10^{-8}$ and $\sim 10^{-7}$ mbar for the *ex-situ* investigation and the *in-situ* investigation, respectively. Note that the very same ion source has been used in the *ex-situ* and the *in-situ* experiments. The sample temperature during the experiments was always below 200°C so that no recrystallisation of the amorphous layer is expected. The applied ion flux was determined by measuring the ion current on the sample and ranged from 3.5×10^{14} to 3.5×10^{15} $\mathrm{cm}^{-2}\mathrm{s}^{-1}$. Within this range, no influence of the flux on the surface morphology was observed. No suppression of secondary electrons has been performed since previous measurements [85] indicated only a minor importance of secondary electron emission under the current experimental conditions. In addition, since the here presented experiments investigate the evolution of the surface morphology, the results of this work are not affected by the absolute fluence values. In the following, the working principles of the Kaufman ion source and the atomic force microscope as well as the fundamentals of grazing incidence small angle X-ray scattering shall briefly be described.

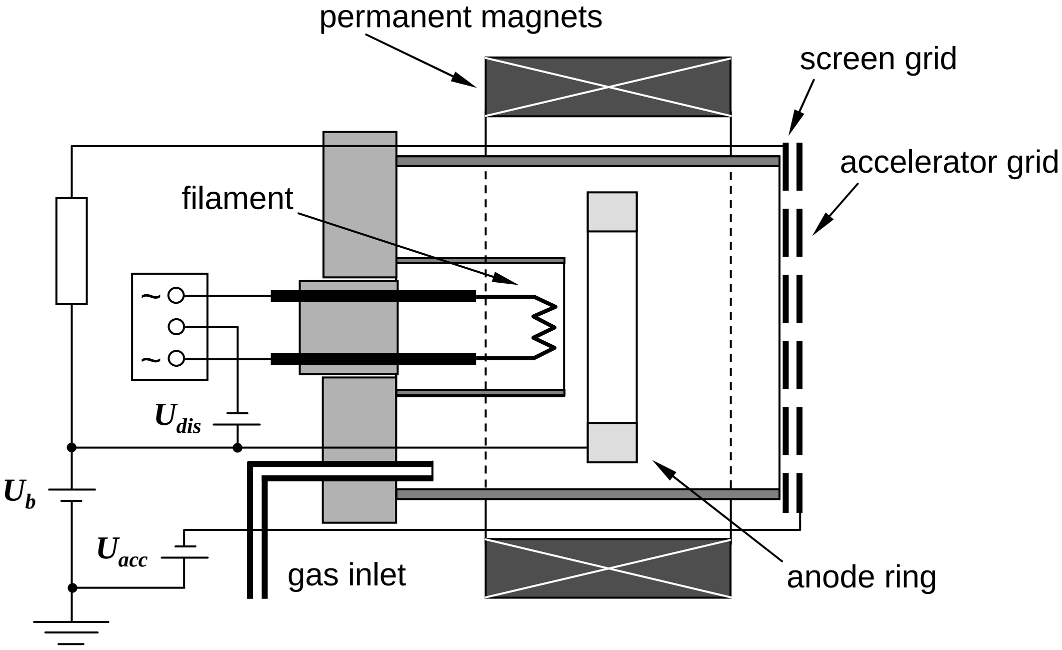

Figure 5.1: Schematic drawing of the Kaufman ion source.

5.1 Kaufman ion source

In this work, a high-flux Kaufman type ion source [86,87] has been used for the sputtering. This type of ion source was originally developed for electric space propulsion and has become a standard ion source in many industrial processes, e.g. in ion beam assisted deposition [88] or surface smoothing [89]. The main components of the Kaufman ion source are shown in Fig. 5.1. A hot tungsten filament emits electrons into the discharge chamber that is flooded with a noble or inert gas. These electrons are accelerated towards an anode ring by applying a positive voltage, the so-called discharge voltage U_{dis}, between filament and anode. The electrons are confined by a magnetic multipole field in which they move on spiral trajectories. This prevents the electrons from reaching the anode except by diffusion. Neutral gas atoms get ionized due to collisions with the energetic electrons and a plasma is created in the discharge chamber. From this plasma, ions are extracted through a double grid system consisting of the screen and the accelerator grid. Each grid consists of hexagonally ordered holes of 1 mm diameter and has an opening aperture of two inches in diameter. The grids as well as the anode ring are made of carbon.

The energy of the extracted ion beam (represented by the so-called beam voltage U_b) is determined by the sum of U_{dis} and the voltage U_{scr} applied to the screen grid, $U_b = U_{dis} + U_{scr}$. By applying a negative voltage U_{acc} to the accelerator grid, ions get extracted from the plasma and are accelerated towards this grid. The value of U_{acc} affects the shape and the divergence of the ion beam. However, in the current experiments, no influence of U_{acc} on the surface morphology has been observed. The same holds also for the discharge voltage U_{dis}. Therefore, in the experiments of this work, U_{acc} was fixed at -200 V and U_{dis} at ~ 100 V. The working pressure in the vacuum chamber during operation was $\sim 2 \times 10^{-4}$ mbar.

From the working principle of the Kaufman ion source, it is clear that the extracted ion beam is contaminated with tungsten from the filament and carbon from the grids. In addition, if the sample is smaller that the beam diameter, sputtered material from the sample holder or the vacuum chamber might get deposited on the sample surface leading to additional metal contaminations. However, for the samples of the current work, Rutherford backscattering spectroscopy (RBS) measurements showed only minor contaminations of less than one monolayer on the sputtered surfaces.

5.2 Atomic force microscopy

Since its invention in 1986 by Binnig *et al.* [90], the atomic force microscope (AFM) has become a popular tool for the investigation of nanoscale and atomic features on various surfaces [91,92]. An AFM essentially consists of a very sharp tip mounted on a cantilever that is scanned across the sample surface. In virtually all AFM systems, piezoelectric scanners with high lateral precision are used [93]. When approaching the surface, the tip becomes subject to several attractive and repulsive interatomic forces [92]. This results in a macroscopic bending of the cantilever. In commercial AFM systems, this bending is usually measured by the deflection of a laser beam that is reflected from the backside of the cantilever.

Depending on the type of force that is acting on the tip, one usually distinguishes three operation types in atomic force microscopy. When the AFM is operated in **contact mode**, the tip is so close to the sample surface that the interaction between tip and surface is strongly influenced by the short distance repulsive forces caused by the Pauli exclusion. However, due to capillary or adhesive forces, the net interaction can still be of attractive nature. In the **non-contact mode**, the cantilever is vibrated near its resonant frequency with an amplitude up to some ten nanometers. Since the distance between tip and surface is slightly larger than the amplitude, the interaction is fully governed by long range attractive van der Waals forces. Depending on sample and tip, however, electrostatic and magnetic forces (attractive and repulsive) may also contribute. Force variations result in changes of the resonant frequency or the vibration amplitude and can, therefore, be detected. **Intermittent-contact** or **tapping mode** atomic force microscopy is similar to the AFM operation in the non-contact mode, except that the vibrating cantilever is brought closer to the surface. Thus, at the bottom of each travel, the tip probes also the repulsive forces; it 'taps' the surface.

All the AFM measurements of this work have been performed in air using a MultiMode™ scanning probe microscope with a NanoScope IV controller from Veeco Instruments in tapping mode. Images were usually taken with 1024 points per scan line. PointProbe® Plus tips (PPP-NCLR) for non-contact and tapping mode operation from NANOSENSORS™ have been used. These tips are shaped like polygon based pyramids of 10 to 15 μm height. The tip apex has a radius typically smaller than 7 nm and a half cone angle of less then 10°. The cantilevers are made of highly doped silicon with a reflective aluminum coating on the detector side and have a nominal length of 225 μm.

In order to determine the dynamic scaling behavior of the imaged surface, the one-dimensional structure factors in the direction normal and parallel to the ion beam, respectively, have been calculated from the AFM images according to equation (4.6). This is demonstrated in Fig. 5.2 which shows the AFM image of a sputtered Si(100) surface (Fig. 5.2(a)) and the corresponding structure factor curves $S_{n,p}(k_{n,p})$ (Fig. 5.2(b)). The $S_n(k_n)$ $(S_p(k_p))$ curve was obtained by calculating the one-dimensional structure factor of every row (column) of pixels of the image in Fig. 5.2(a) and subsequent averaging over the single rows (columns). In order to minimize the influence of measurement artifacts, the structure factor curves used in the scaling analysis of chapter 6.2 have then been averaged over six AFM images taken at different positions on the surfaces of up to five identically treated samples.

5.3 Grazing incidence small angle X-ray scattering

The *in-situ* investigations of the surface evolution have been performed at the bending magnet beam line BM5 at the European Synchrotron Radiation Facility (ESRF) in Greno-

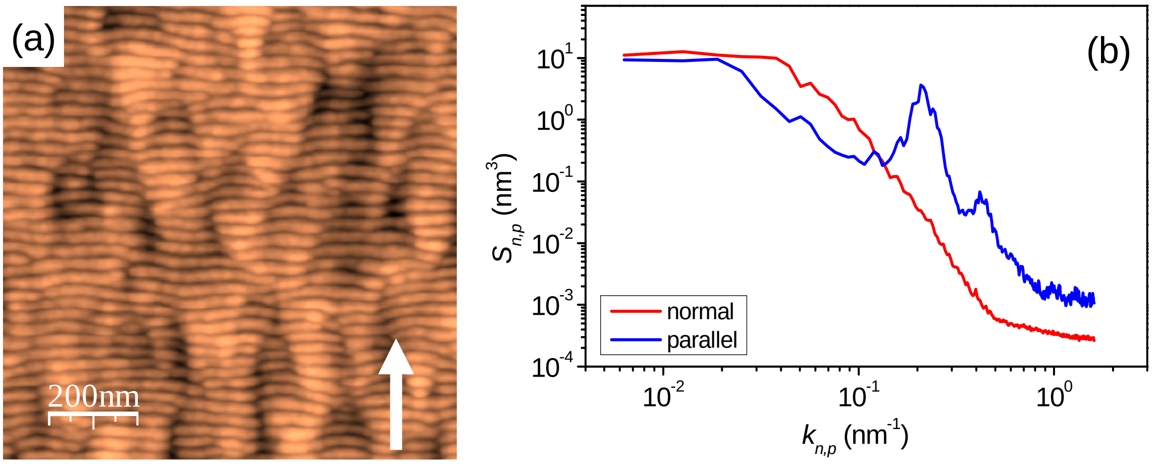

Figure 5.2: (a) AFM image of Si(100) surface sputtered with 500 eV Ar^+ ions under 67° incidence at a fluence of 5×10^{17} cm^2. The white arrow gives the beam direction. (b) Corresponding one-dimensional structure factor curves in the direction normal (red) and parallel (blue) to the direction of the ion beam, respectively.

ble, France. The BM5 beam line is dedicated to the fabrication and characterization of super-smooth surfaces, thin films, and multilayers for the application in X-ray optics. Therefore, this beam line is equipped with a sophisticated setup for the *in-situ* and real-time investigation of surfaces during their processing under high-vacuum conditions. A scheme of the experimental setup as used in the present work is given in Fig. 5.3. In this geometry, the ripples form normal to the direction of the ion beam and, therefore, parallel to the direction of the incident X-ray beam.

The GISAXS technique measures diffuse scattering at rough surfaces under grazing incident and exit angles. It is not sensitive to the crystalline structure of the surface but only to the contrast in electron density and, therefore, to variations of the refractive index. This way, information about correlations in the surface roughness can be obtained. The experiments of this work have been performed at a fixed incident angle of $\theta = 0.3°$ with respect to the surface and an X-ray energy of 17.5 keV. The diffuse scattering has been monitored using a cryogenically cooled charge coupled device (CCD) camera with 1024×256 pixels and a pixel size of 19 μm. In order to avoid saturation of the camera, the specular beam has been blocked by a beam stop.

Fig. 5.4 shows a scattering diagram as recorded after sputtering a Si(100) surface with

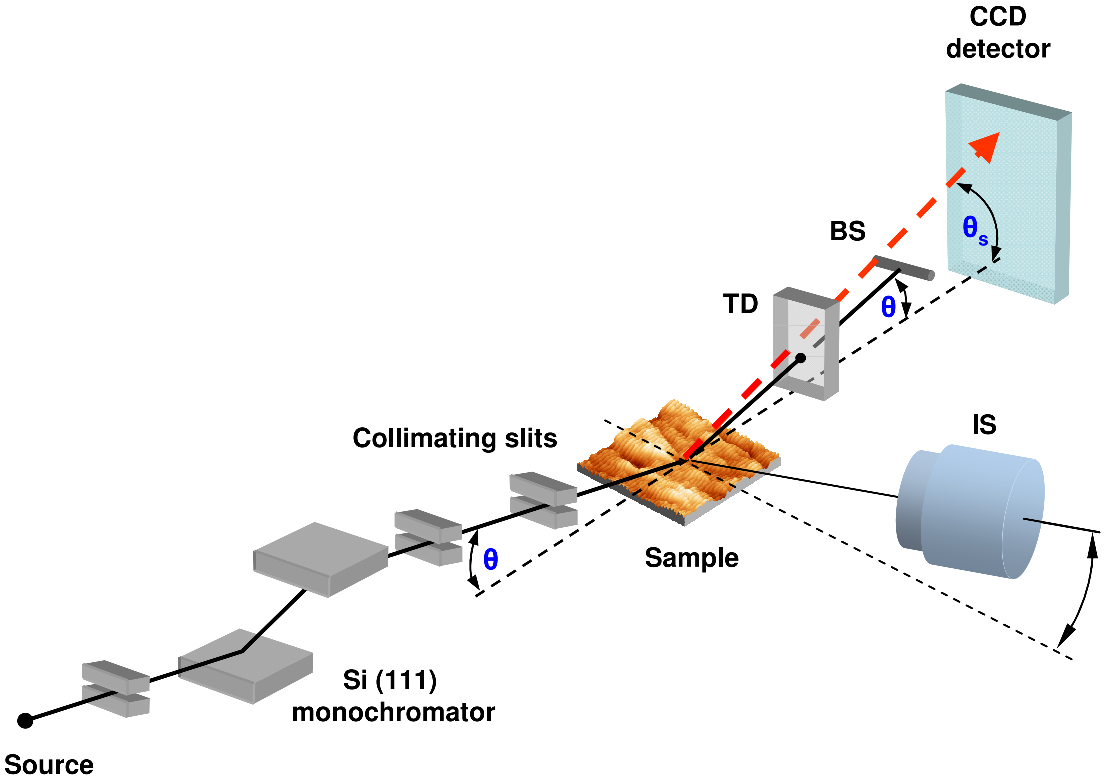

Figure 5.3: Experimental setup at the ESRF beam line BM5 with ion source IS, beam stop BS, and transmission detector TD.

1.7×10^{18} 500 eV Ar ions per cm^2 under 67° incidence. One can clearly see the satellite peaks that correspond to the spatial frequency k_c of the ripple pattern. From such a scattering diagram, one-dimensional cuts $S_{n,p}$ of the two-dimensional structure factor of the surface can be extracted in the direction normal and parallel to the ion beam. For this, intensity cuts $\Pi_{n,p}$ of the scattering diagram have been taken along the lines shown in Fig. 5.4. In the direction parallel to the ion beam, the cut Π_p (white line in Fig. 5.4) is directly proportional to the structure factor S_p. In the direction parallel to the ion beam, however, the cut Π_n (black line in Fig. 5.4) is related to the structure factor S_n by [94]

$$\Pi_n(\theta_s) = \frac{p^3 \left|(1-\epsilon)\, g(\theta)\, g(\theta_s)\right|^2}{16\pi \sin(\theta)} S_n(k_n) \tag{5.1}$$

with the scattering angle θ_s, the wave number p of the incident X-ray light, the spatial

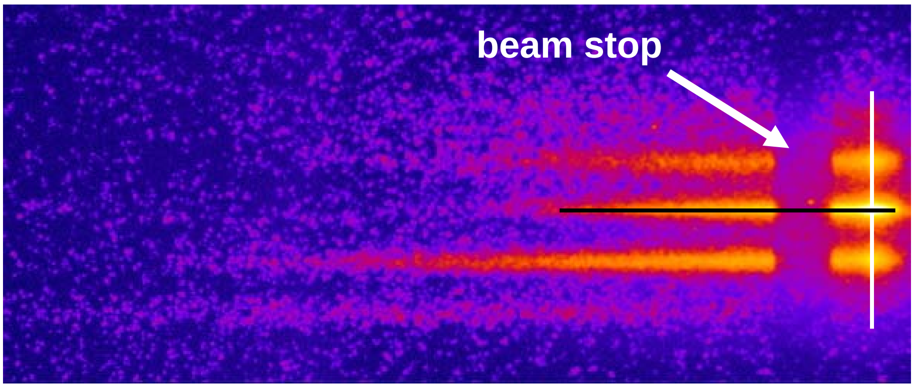

Figure 5.4: Scattering diagram of Si(100) after sputtering with 500 eV Ar^+ ions under 67° ion incidence at a total fluence of 1.7×10^{18} cm^{-2}.

frequency k_n, the dielectric function of silicon ϵ, and the function

$$g(\theta) = \frac{2\sin(\theta)}{\sin(\theta) + \sqrt{\epsilon - \cos^2(\theta)}}. \tag{5.2}$$

For an anisotropic surface, the so extracted one-dimensional cuts of the two-dimensional structure factor follow the same scaling relations as the one-dimensional structure factors [84]. Thus, one can determine the dynamic scaling properties of the surface in the direction normal and parallel to the ion beam, respectively, as described in chapter 4. However, this approach has the disadvantage that different regions in k space are probed in the different directions. Therefore, the one-dimensional local interface widths cannot be measured reliably. Nevertheless, the two-dimensional local interface width w can be easily estimated from the total integrated scattering (TIS) by the relation [95]

$$w(t) \sim \frac{1}{2p\sin(\theta)} \sqrt{\frac{\mathrm{TIS}(t)}{R_\Sigma(t)}} \tag{5.3}$$

with R_Σ being the total Fresnel reflectivity. One should note, however, that this method for determining w is very sensitive to the alignment of the sample and the X-ray beam and, therefore, causes rather large uncertainties of the w values.

Chapter 6

High-Fluence Ion Sputtering of Silicon Surfaces

In the linear regime of pattern evolution, all the current nonlinear continuum models described in section 2.3 behave similar to the linear BH equation. For the nonlinear regime, however, the different models make different and sometimes contradictory predictions. Therefore, a distinct demand for high fluence experiments has developed which investigate the evolution of the surface morphology in the nonlinear regime. In this chapter, the morphology evolution of silicon surfaces during high-fluence low-energy ion sputtering shall be presented and discussed with respect to different nonlinear continuum models.

6.1 Formation of two ripple modes

In order to study the evolution of the surface morphology during high-fluence ion sputtering, Si(100) samples were sputtered with Ar ions of 300 and 500 eV energy at different fluences. The angle of incidence was $\theta_{ion} = 67^\circ$ with respect to the surface normal. The applied fluence ranged from 5×10^{16} to 1×10^{20} cm^{-2} and from 1×10^{17} to 5×10^{19} cm^{-2} for 500 and 300 eV, respectively. Fig. 6.1(a-c) shows corresponding AFM images obtained after 300 eV bombardment: at low fluence (Fig. 6.1(a), $\Phi = 1 \times 10^{17}$ cm^{-2}), the surface exhibits a pattern of shallow ripples oriented *normal* to the ion beam projection. In the following this pattern is called *normal pattern*. The two-dimensional Fourier transform (FFT) of this image (see inset of Fig. 1(a)) shows two clearly separated side peaks. The position of the side peaks corresponds to the periodicity of the pattern, yielding a nor-

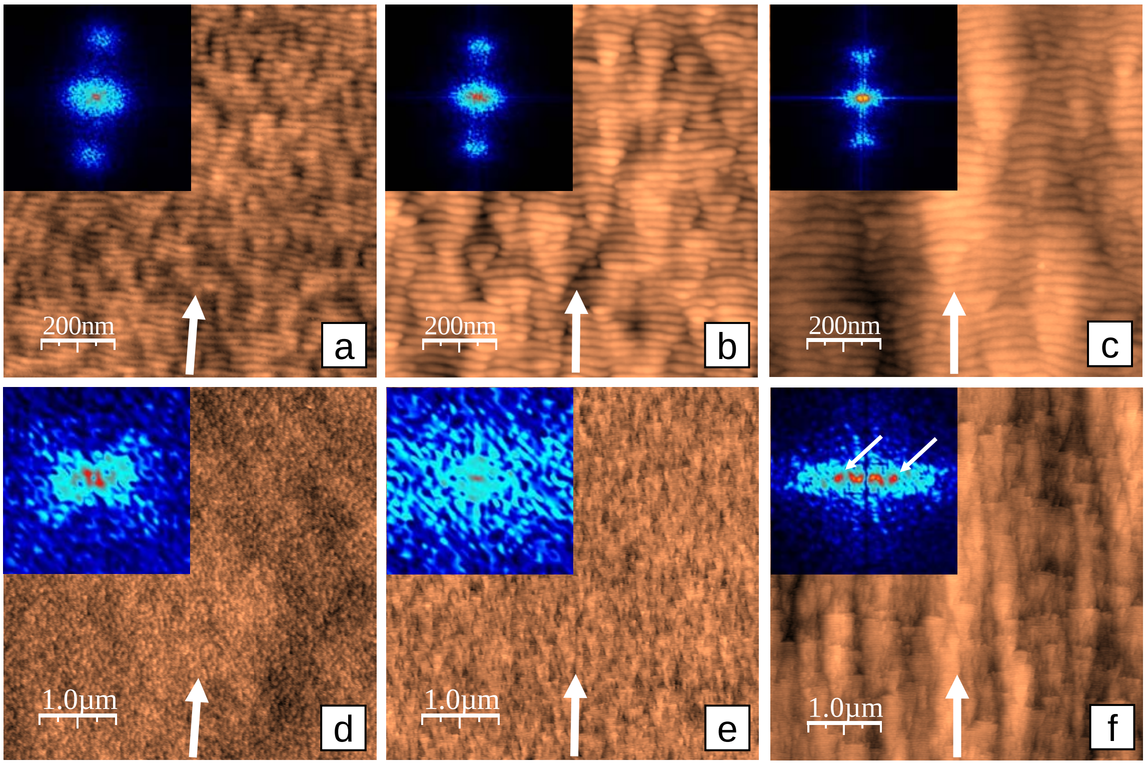

Figure 6.1: AFM images of Si(100) after sputtering with 300 eV Ar^+ ions at fluences $\Phi = 1 \times 10^{17}$ (a,d), 5×10^{17} (b,e), and 1×10^{19} cm^{-2} (c,f). Intensity scales are 7 nm (a), 10 nm (b), 16 nm (c), 8 nm (d), 13 nm (e), and 28 nm (f). The white arrows indicate the beam direction. Insets: corresponding FFT ranging from -75 to +75 $\mu\mathrm{m}^{-1}$ (a-c) and from -4 to +4 $\mu\mathrm{m}^{-1}$ (d-f).

mal wavelength $\lambda_n \sim 20$ nm. With increasing fluence (Fig. 6.1(b), $\Phi = 5 \times 10^{17}$ cm^{-2}), corrugations overlay the normal pattern and get more pronounced until they become the dominating feature of the surface (Fig. 6.1(c), $\Phi = 1 \times 10^{19}$ cm^{-2}). At higher fluences, the surface reaches a steady state with reduced order and quality of the normal ripples.

Larger area AFM scans (Fig. 6.1(d-f)) reveal that the corrugations overlaying the normal pattern become anisotropic with increasing fluence and finally form a quasi-periodic pattern at high fluences, which is oriented *parallel* to the beam direction (Fig. 6.1(f)). This pattern is referred to as *parallel pattern*. Although the parallel pattern exhibits a much lower degree of order, side peaks can be identified (indicated by the white arrows) in the

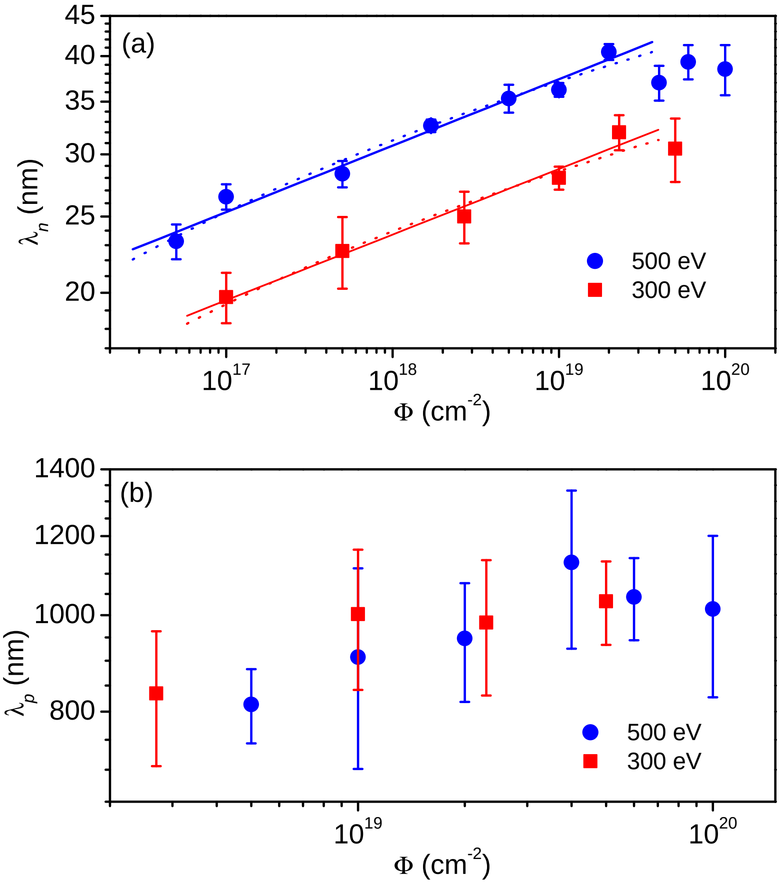

Figure 6.2: Evolution of (a) normal wavelength λ_n and (b) parallel periodicity λ_p at 300 eV and 500 eV. The solid lines in (a) represent power law fits, yielding coarsening exponents of $n = 0.085 \pm 0.006$ and $n = 0.084 \pm 0.007$ for 500 eV and 300 eV, respectively. The dotted lines represent logarithmic fits.

FFT, as shown in the inset of Fig. 6.1(f). The side peaks indicate the quasi-periodicity of the parallel pattern and their position yields a much larger spatial periodicity of $\lambda_p \sim 900$ nm.

In Fig. 6.2(a) the fluence dependence of the normal wavelength λ_n, determined from the FFT of each AFM image, is depicted. It can be seen that λ_n increases with the fluence Φ until it saturates at $\Phi \sim 10^{19}$ cm^{-2}. The solid lines in Fig. 6.2(a) represent

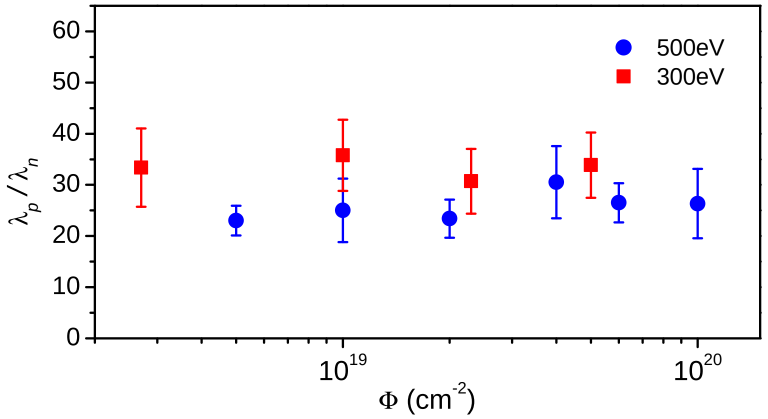

Figure 6.3: Ratio of parallel to normal periodicity λ_p/λ_n over fluence for 300 eV and 500 eV.

power law fits, $\lambda_n \propto \Phi^n$, with a coarsening exponent $n \sim 0.08$. Note, however, that the data can as well be fitted by logarithmic functions, $\lambda_n \propto \log \Phi$ (dotted lines in Fig. 6.2(a)). In addition, λ_n decreases with ion energy, indicating that ion-induced diffusion is the dominating smoothing process (cf. chapter 2.3.3). This is also in agreement with the observed independence of λ_n of the ion flux. The first parallel ripples with distinguishable periodicity were observed at $\Phi = 5 \times 10^{18}$ and $\Phi = 2.3 \times 10^{18}$ cm^{-2} for 500 and 300 eV, respectively. The evolution of λ_p is shown in Fig. 6.2(b). Again, coarsening with increasing Φ is observed. Fig. 6.3 depicts the ratio of the periodicities λ_p/λ_n. This ratio is quite constant in the investigated fluence range, indicating that both ripple modes exhibit similar coarsening behavior.

The evolution of the local interface width w as obtained from the AFM images is shown in Fig. 6.4. For both ion energies, w increases following a power law until it saturates at high fluences. For the higher energy, this saturation is reached earlier. This can probably be attributed to the higher erosion rate at this energy. Interestingly, the value of the saturated interface width is significantly larger for the lower energy. A similar behavior has already been observed for oxygen sputtering of silicon [96]. For both energies, power law fits yield a similar growth exponent $\beta \sim 0.27$.

One should note that the local interface width is not determined by the amplitude of

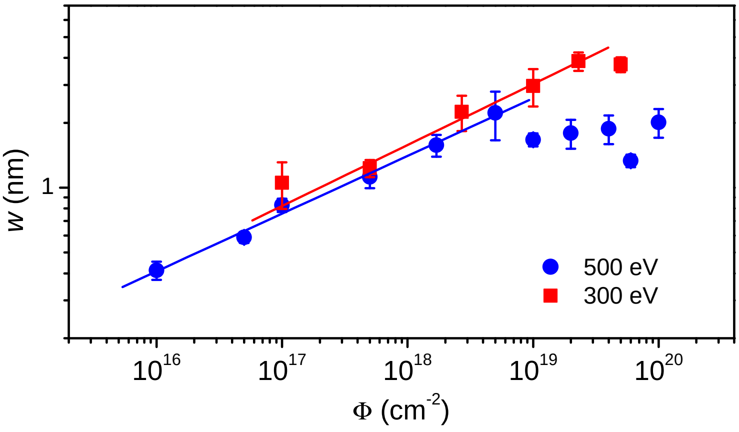

Figure 6.4: Local interface width w vs. fluence. The solid lines represent power law fits, yielding growth exponents of $\beta = 0.28 \pm 0.03$ and $\beta = 0.27 \pm 0.02$ for 500 eV and 300 eV, respectively.

the normal ripple pattern but rather by the larger corrugations and the parallel pattern, respectively. This is shown in Fig. 6.5 that depicts the evolution of the ripple amplitude a, defined as the half of the average peak-to-peak height of the ripples, for the case of 500 eV sputtering. In the low fluence regime, the amplitude a is increasing from initially 0.4 nm to a maximum value of about 0.8 nm at $\Phi \simeq 5 \times 10^{17}$ cm^{-2}. For higher fluences, the amplitude decreases again and finally saturates at a value of $a^{sat} \simeq 0.6$ nm. A similar overshooting before saturation has already been observed in previous experiments under normal ion incidence [28] and simulations of the anisotropic KS equation [25]. Comparison with the evolution of the local interface width as given in Fig. 6.4 shows that the local interface width still increases long after the ripple amplitude has saturated.

There are several studies investigating the evolution of ion-induced ripple patterns on silicon. For near-normal ion incidence, Ziberi *et al.* observed the formation of ripples with constant wavelength [29]. On the contrary, other experiments showed no pattern formation at low incidence angles [8, 33, 97] what agrees with the current experimental observations where the surface remained flat at near-normal incidence. Nevertheless, studies of the hydrodynamic model of ion erosion (see chapter 2.3.4) pointed out that

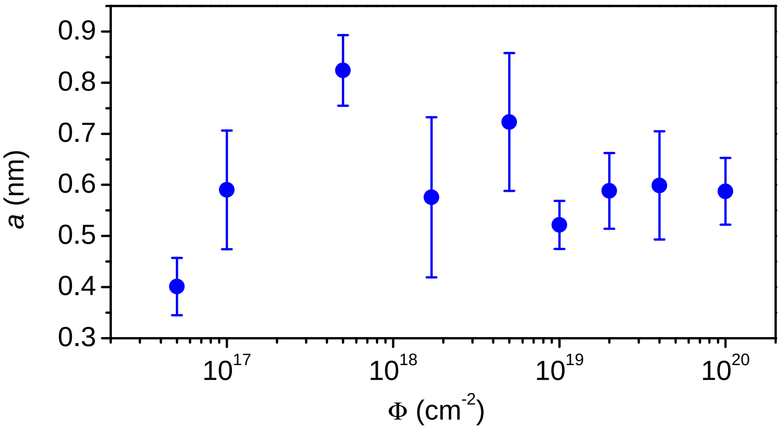

Figure 6.5: Evolution of the ripple amplitude a versus fluence for 500 eV.

the coarsening of the ripple wavelength depends on the values and relative signs of the nonlinear coefficients and, therefore, also on the angle of incidence [38, 69].

Although similar morphologies as presented here were found in experiments done under nearly identical conditions at low and intermediate fluences by Alkemade *et al.*, stronger coarsening of the ripples was observed [31]. However, O_2^+ ions have been used for the sputtering. This affects the chemistry of the Si surface and could therefore also influence the dynamics of the patterns. Other studies of the evolution of rippled silicon surfaces at low [98] and high [33] ion energies report the formation of faceted, sawtooth-like structures at high fluences that probably result from geometrical shadowing. The corrugations observed in the present experiments, however, do not exhibit a sawtooth-like shape. This indicates that shadowing effects do not play a role in this experimental system (67° incidence, $\sim$ 1.5 nm ripple height). This is in agreement with general geometrical considerations [99].

In recent experiments performed at elevated temperature (i.e. with isotropic thermal diffusion dominating the surface relaxation), Brown *et al.* observed transient topographies on the crystalline Si(111) surface [44, 53]. In a transition regime, an initial ripple pattern oriented normal to the beam direction is superposed by a parallel ripple pattern. The normal pattern soon vanishes, resulting in a pattern rotation. In contrast to these findings, no transition regime is observed in the experiments presented here. Even for the highest fluence of 1×10^{20} cm^{-2} both patterns are still present. Moreover, the normal pattern is not expected to decay any further at higher fluences because the surface enters a steady state already at a fluence of 10^{19} cm^{-2}. In the high temperature experiments, exponential coarsening of both ripple modes was observed and attributed to the step edge dynamics of the crystalline surface [53]. In contrast and as described above, the experiments of the present work were performed at moderate temperature, leading to an immediate amorphization of the Si surface due to ion impact. Therefore, this interpretation offers no suitable explanation for the present findings. The here presented observations rather suggest that coarsening of both normal and parallel ripples is an inherent feature of the sputtering process.

6.2 Anisotropic scaling behavior

In order to further characterize the surface morphology, the dynamic scaling behavior of the Si surface during sputtering at 500 eV has been investigated. For this, the structure factor $S(k,t) = \left\langle \tilde{h}(k,t)\tilde{h}(-k,t) \right\rangle_\eta$ of the surface has been evaluated at the different fluences. Since the observed surface morphology is highly anisotropic, the one-dimensional structure factor $S_{n,p}(k_{n,p})$ has been calculated in the direction normal and parallel to the projected direction of the ion beam, respectively, as described in section 5.2.

In Fig. 6.6(a), the structure factor curves in the direction normal to the ion beam, $S_n(k_n)$, are depicted for different fluences. At large values of k_n, the S_n curves all collapse. The slope m (in the log-log plot) of the curves in this regime is about -4, corresponding to a roughness exponent of 1.5 (cf. equation (4.22)). At small k_n values, however, $S_n(k_n)$ increases with fluence and a second scaling regime develops. The roughness exponent in this long-range scaling regime is $\alpha_n = 0.76 \pm 0.04$. For high fluences $\Phi > 10^{19}$ cm^{-2}, the S_n curves collapse also at low k_n. However, at lowest k_n values, a slight rounding of the structure factor curves is observed even for the highest fluence applied. This might indicate that the large-scale morphology has not fully saturated yet.

The structure factor $S_p(k_p)$ calculated in the direction parallel to the ion beam is given in Fig. 6.6(b). In this direction, for $\Phi \geq 5 \times 10^{16}$ cm^{-2}, a peak appears at the spatial frequency k_p^* corresponding to the wavelength λ of the ripple pattern. For $k_p \gg k_p^*$, the data is consistent with a slope $m = -4$. With increasing fluence, the ripples coarsen and the position of the peak is shifting to smaller k_p values. As in the direction normal to

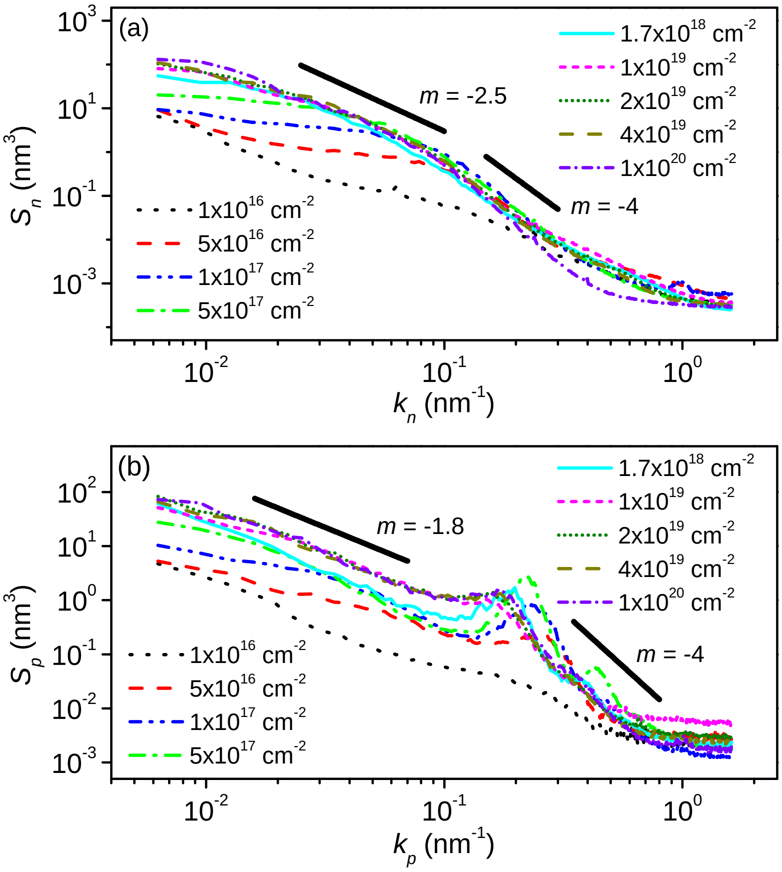

Figure 6.6: Structure factors $S_{n,p}(k_{n,p})$ in the direction normal (a) and parallel (b) to the ion beam for Si(100) sputtered at different fluences. The straight solid lines correspond to $S_{n,p} \sim k_{n,p}^m$.

the ion beam, the structure factor increases with fluence for $k_p \ll k_p^*$ and again shows a power-law behavior at high fluences. Here, the roughness exponent was determined to be $\alpha_p = 0.41 \pm 0.04$. As in the n direction, the S_p curves of the highest fluences exhibit a slight rounding at lowest k_p.

Note that the apparent power law behavior of the $S_{n,p}$ curves at low $k_{n,p}$ for the lowest fluence given in Fig. 6.6(a,b) originates from the virgin Si substrate. With increasing fluence, however, the influence of the substrate vanishes.

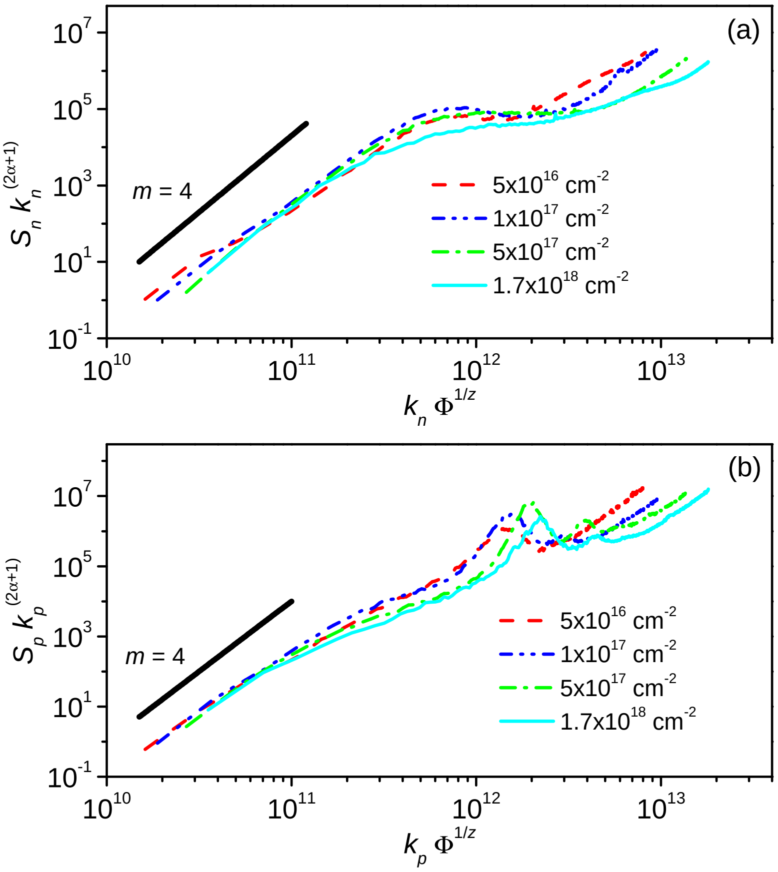

Figure 6.7: Collapsed structure factor curves at low fluences in the direction normal (a) and parallel (b) to the ion beam, respectively. The collapses were obtained using $\alpha_{n,p} = 1.5$ and $z_{n,p} = 4.5$. The straight solid lines have a slope m.

From equations (4.7) and (4.8) it follows that plotting the rescaled structure factor $S(k,t)k^{(2\alpha+1)}$ versus $kt^{1/z}$ for the different times, all curves should collapse into a single one. In this way, the dynamic exponents $z_{n,p}$ can be measured by using the previously determined roughness exponents $\alpha_{n,p}$. Fig. 6.7(a,b) shows the collapsed structure factor curves for low fluences. In both directions, a good collapse is obtained for $\alpha_{n,p} = 1.5$ and $z_{n,p} = 4.5$. The low-$k_{n,p}$ slope of the collapsed structure factor curves should be given by $m = 2\alpha_{n,p} + 1 = 4$. This behavior is reasonably well confirmed as can be seen from the straight solid lines in Fig. 6.7.

The observed peak in the structure factor S_p in the direction parallel to the ion beam with the -4 slope at large k_p values (cf. Fig. 6.6(b)) indicates the presence of a KS like instability in this direction [26]. The orientation of the ripples with respect to the incident ion beam is determined by the signs of the linear coefficients: the wave vector of the observed ripple structure is parallel to the direction with the smallest negative ν (cf. chapter 2.2). Therefore, for the here presented experiment $\nu_p < \nu_n$. Concerning the value of ν_n, three cases can be distinguished, as follows from the exact form of $S(k,t)$ for the linear BH equation, that is accurate for small time and length scales. Note that in principle the very short-distance behavior of equation (2.26) is dominated by the diffusion term, inducing the scaling behavior of the linear MBE equation (4.15), whose exponent values in (1+1) dimensions are $\alpha_{MBE} = 3/2$ and $z_{MBE} = 4$ (cf. table 4.1).

(i) $\nu_n > 0$. For a sizeable and positive ν_n the scaling behavior should cross over from linear MBE to EW type [39], the power characterizing the $S_n(k_n)$ decay with k_n clearly departing from the -4 value at intermediate time and length scales.

(ii) $|\nu_n| \approx 0$. For $|\nu_n|$ close to zero, no transition to EW scaling will occur and the 1D linear MBE exponents will be valid even for long times.

(iii) $0 > \nu_n > \nu_p$. A negative ν_n value will introduce a second instability in the n direction. Although the instability in the p direction will overcome this second instability very soon, the corresponding structure factor S_n will exhibit a local maximum at $k_n^* = \sqrt{|\nu_n|/2D}$. However, for $|\nu_n| \ll |\nu_p|$, the local maximum might be too small to be recognized in the structure factor curve.

The experimental S_n curves shown in Fig. 6.6(a) do not exhibit a local maximum. The determined low-fluence behavior for the n direction $S_n(k_n) \sim k_n^{-4}$ as induced by the diffusion term holds even at the highest applied fluence of $\Phi = 1 \times 10^{20}$ cm^{-2}. Therefore, the second case with $|\nu_n| \approx 0$ appears most likely.

The collapsed structure factor curves at high fluences are shown in Fig. 6.8(a,b). The high-$k_{n,p}$ part of the curves was cut. In the n direction, again a good collapse is obtained. In the p direction, however, the collapse is less perfect. This can be attributed to the fact that the p direction is also the slow-scan direction of the AFM and, therefore, rather sensitive to sampling related artifacts especially at long wavelengths. Nevertheless, the obtained collapse is still reasonable as is indicated again by the straight black lines in Fig. 6.8(a,b) that have slopes of $m = 2\alpha_n{+}1 = 2.52$ and $m = 2\alpha_p{+}1 = 1.82$, respectively. After the system reached its stationary state, one expects $\beta = \alpha_{n,p}/z_{n,p} = 0$ (see equations (4.2)

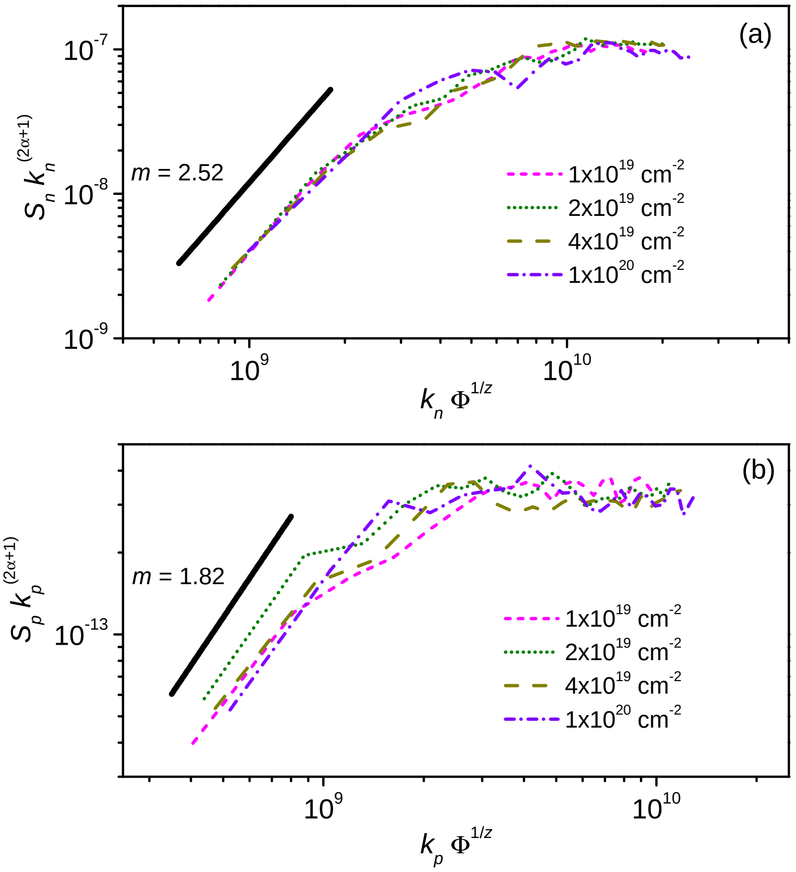

Figure 6.8: Collapsed structure factor curves for $k_{n,p} \ll k_p^*$ at high fluences in the direction normal (a) and parallel (b) to the ion beam, respectively. The collapses were obtained using $\alpha_n = 0.76$, $z_n = 8$, $\alpha_p = 0.41$, and $z_p = 9$. The straight solid lines have a slope m.

and (4.3)) and, therefore, very large effective $z_{n,p}$ values, $z_{n,p} \to \infty$. The data collapses shown in Fig. 6.8, however, were obtained for $z_n = 8$ and $z_p = 9$. Although these values are by a factor of 2 larger than the ones obtained at low fluences and large $k_{n,p}$, they are still of comparable magnitude and not close to infinity. This supports the interpretation that the system is not saturated yet as already indicated by the rounding of $S_{n,p}(k_{n,p}, t)$ at small $k_{n,p}$ for the highest fluences (cf. Fig. 6.6). However, no final conclusions on that issue can be drawn from the current data set.

Although the long-range scaling behavior of the anisotropic KS equation (2.26) is still unexplored, two different long-time scaling regimes are expected depending on the relative signs of the nonlinear coefficients ζ_n and ζ_p. For $\zeta_n\zeta_p > 0$, an algebraic scaling behavior similar to the KPZ equation (2.31) is expected whereas $\zeta_n\zeta_p < 0$ might result in isotropic logarithmic scaling [24, 34]. However, for $\zeta_n\zeta_p < 0$ the appearance of rotated ripples (so-called cancellation modes) has been observed (see chapter 3.1).

For the current experimental conditions, one would expect $\zeta_n\zeta_p < 0$ (see equations (2.27) and (2.28)). However, even for the highest applied fluence of $\Phi = 1 \times 10^{20}$ cm^{-2}, neither the appearance of rotated ripple structures nor isotropic logarithmic scaling is observed. On the contrary, for $\Phi \geq 10^{19}$ cm^{-2}, the morphology exhibits anisotropic algebraic scaling at large length scales with $\alpha_n = 0.76 \pm 0.04$ and $\alpha_p = 0.41 \pm 0.04$. Although these exponents agree fairly well with the exponents found for the isotropic KS equation [70] (early-time regime) and the isotropic KPZ equation [39], respectively, the strong degree of anisotropy in the system rather suggests that this similarity is just coincidental.

In equation (2.26), the only term breaking the $x \to -x$ symmetry is the one with parameter γ. However, in order to fully describe the nonlinear evolution of ion sputtered surfaces, the general continuum equation (2.33) of ion erosion was derived by Makeev *et al.* [34]. In this model, dispersive nonlinearities with coefficients $\xi_{n,p}$ appear. Due to the additional nonlinearities, this general equation has a rather complex parameter space and different scaling behaviors may be expected depending on the nonlinear coefficients. Although the dynamic scaling exponents of equation (2.33) still have to be clarified, additional information from a different particular case of this equation is available [100]. Schmittmann *et al.* [84] have performed a renormalization group calculation for the (linearly stable) case in which $\nu_{n,p} > 0$, while $\gamma = \Omega_n = \Omega_p = \zeta_{n,p} = 0$. Remarkably, they find parameter regimes in which the stationary state is characterized by strong anisotropy, in the sense that $\chi_{n,p} \neq 1$ and thus $\alpha_n \neq \alpha_p$ (see chapter 4.4).

Another experimental observation that can be explained neither with the KS nor with the general equation is the coarsening of the ripple wavelength. However, the recent hydrodynamical model (cf. chapter 2.3.4) developed by Muñoz-García and coworkers is able to show ripple coarsening at intermediate times [38, 68, 69]. In this model, the additional conserved KPZ nonlinearities are seen to induce the coarsening of the ripples at intermediate times. At long times, however, the nonconserved KPZ nonlinearities become dominant and coarsening stops [68, 69]. In this regime, the surface shows dynamic scaling at large lateral scales while conserving the ripple pattern at small scales [69]. Since the transition to this regime is induced by the nonconserved KPZ terms, it is accompanied by a saturation of the ripple amplitude [68, 69]. In the present experimental results, however, coarsening is observed even after the ripple amplitude has saturated (cf. Fig. 6.2 and 6.5). This again might indicate the relevance of the additional nonlinearities $\xi_{n,p}$ [100], whose dynamical role has not been completely assessed (other than, e.g. their contribution to ripple motion with a nonuniform velocity) [68], or perhaps the relevance of relaxation mechanisms other than those considered in two-field models [101]. Nevertheless, one is naturally led to considering the hydrodynamic model as a potential continuum description of the present experiments.

6.3 Dependence on the angle of incidence

An important experimental parameter which is known to significantly influence the surface morphology and evolution is the angle of ion incidence (see e.g. references [8] and [30]). Recently, it was even shown that small variations in the angle of incidence can induce a transition from ripple to tetragonally ordered dot patterns [43]. In addition, different continuum models make certain predictions on the influence of the incident angle on the dynamic scaling [24] and the coarsening behavior [38, 68] of the ripple morphologies. Therefore, the dynamic scaling behavior of the Si(100) surfaces has been studied *in-situ* during sputtering at slightly different incident angles. In these experiments, the Si(100) samples have been sputtered with a constant (corrected) surface flux of 1.4×10^{15} Ar^+ ions per $\mathrm{cm}^2\mathrm{s}$. The ion energy was fixed at 500 eV and the incident angle θ_{ion} was varied between 65° and 69° with respect to the surface normal. The sputtering has been performed in consecutive steps and the surface morphology has been characterized in-between by grazing incidence small angle X-ray scattering (GISAXS).

The AFM images of the final surface morphologies after sputtering with the highest fluences for three different incident angles are shown in Fig. 6.9. All three surfaces exhibit qualitatively similar ripple patterns oriented normal to the direction of the ion beam. The patterns are overlayed by larger features as observed in the *ex-situ* study (see section 6.1) indicating the presence of kinetic roughening at intermediate length scales. For $\theta_{ion} = 65°$ and $67°$ (Fig. 6.9(a,b)), also these structures appear similar. However, for $\theta_{ion} = 69°$ (Fig. 6.9(c)), the superposed structures are less pronounced and the ripple patterns appears more regular. For even lager angles of incidence, the surface enters

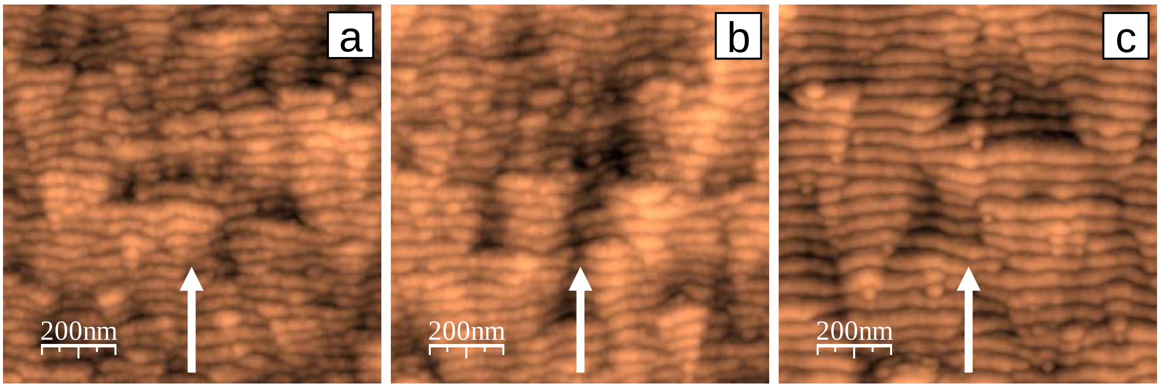

Figure 6.9: AFM images of the Si(100) surfaces after sputtering with the highest fluence at different incident angles: (a) $\theta_{ion} = 65°$, $\Phi = 1.4 \times 10^{19}$ cm^{-2}, (b) $\theta_{ion} = 67°$, $\Phi = 1.6 \times 10^{19}$ cm^{-2}, and (c) $\theta_{ion} = 69°$, $\Phi = 1.6 \times 10^{19}$ cm^{-2}. Intensity scales are 8.5 nm (a), 9 nm (b), and 13 nm (c). The white arrows indicate the beam direction.

a geometrical shadowing regime already at intermediate fluences in which the surface morphology is dominated by faceted, sawtooth-like features similar to those reported in literature [33, 98].

In order to analyze the dynamic scaling behavior of the large scale surface morphology, one-dimensional cuts of the two-dimensional structure factors of the sputtered surfaces have been determined from the scattering diagrams as described in chapter 5.3. Fig. 6.10 shows structure factor curves for 65° ion incidence at different fluences. At low fluences, the roughness of the sample is correlated within the whole k_n range under investigation. This correlation results from the initial surface of the virgin sample. With increasing sputter time, however, another scaling regime develops at high k_n whereas the power spectrum is rounded at low k_n values. This observation supports the previous assumption based on the *ex-situ* AFM data (see section 6.2) that even for the longest sputter times the system has not yet reached its stationary state. From the slope of the structure factor at high k_n, a roughness exponent $\alpha_n = 0.81 \pm 0.05$ has been determined. In the direction parallel to the ion beam (Fig. 6.10(b)), the $S_p(k_p)$ curves exhibit ripple coarsening as indicated by the shift of the local maximum with increasing fluence. For low k_p values, again the development of a scaling regime is observed. The slope of the structure factor curves at long times gives a roughness exponent $\alpha_p = 0.04 \pm 0.02$.

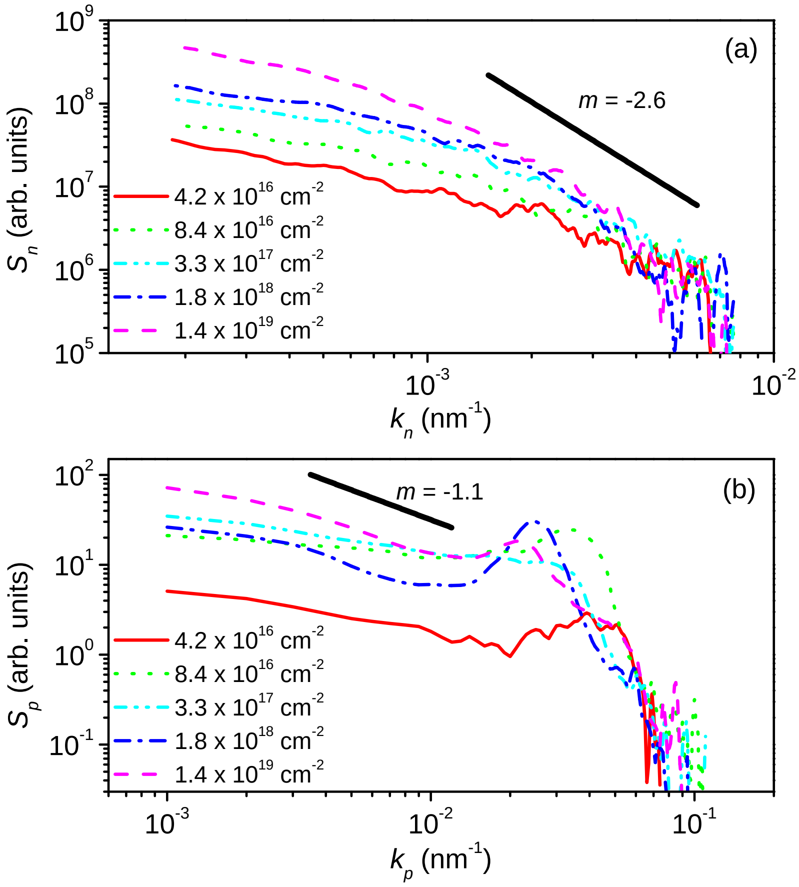

Figure 6.10: Structure factors obtained from the scattering diagrams for 65° ion incidence in the direction normal (a) and parallel (b) to the ion beam. The straight solid lines correspond to $S_{n,p} \sim k_{n,p}^m$.

Fig. 6.11 depicts some structure factor curves $S_{n,p}(k_{n,p})$ of the sample sputtered under 69° incidence at four different fluences. Qualitatively, these curves behave similar to the ones obtained under 65° incidence (cf. Fig. 6.10). However, the roughness exponent determined at highest fluences, $\alpha_n = 0.46 \pm 0.07$, is significantly smaller than for 65° incidence and agrees fairly well with the roughness exponent obtained in the direction parallel to the ion beam, $\alpha_p = 0.49 \pm 0.02$. Therefore, the surface exhibits *isotropic*

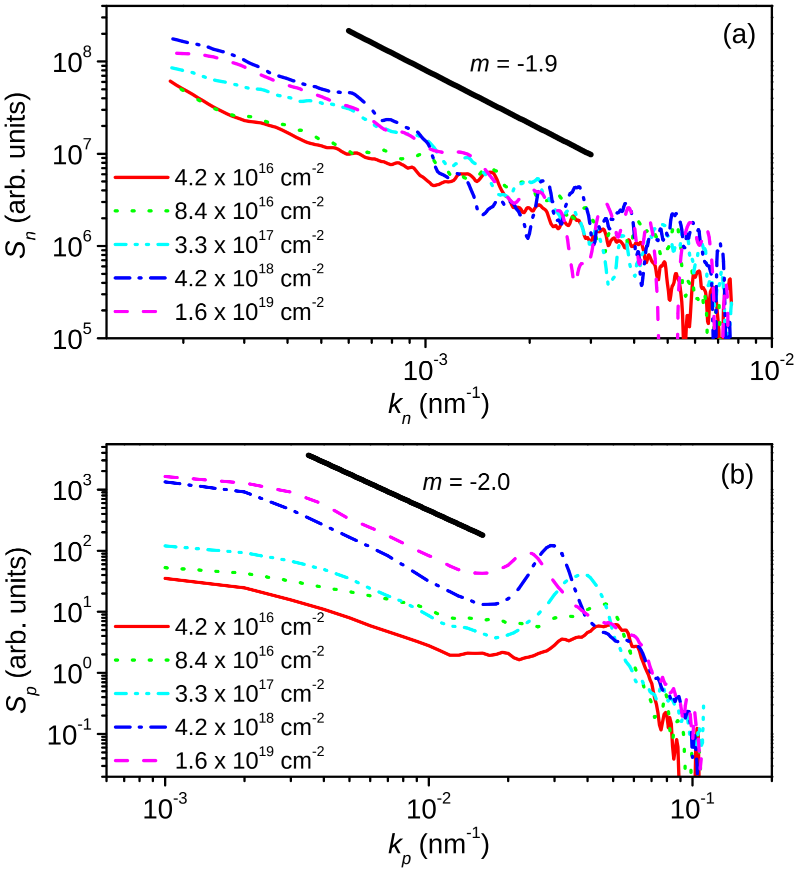

Figure 6.11: Structure factors obtained from the scattering diagrams for 69° ion incidence in the direction normal (a) and parallel (b) to the ion beam. The straight solid lines correspond to $S_{n,p} \sim k_{n,p}^m$.

scaling of the large scale morphology for sputtering under 69° ion incidence.

In order to verify the accuracy of the methods for determining the scaling exponents *in-situ* and *ex-situ*, the experiment for 67° incidence described in the previous sections has been repeated and the scaling exponents have been measured *in-situ* as for the other two incident angles $\theta = 65°$ and $\theta = 69°$. The so determined roughness exponents $\alpha_n = 0.72 \pm 0.05$ and $\alpha_p = 0.42 \pm 0.02$ agree fairly well with the ones obtained under the

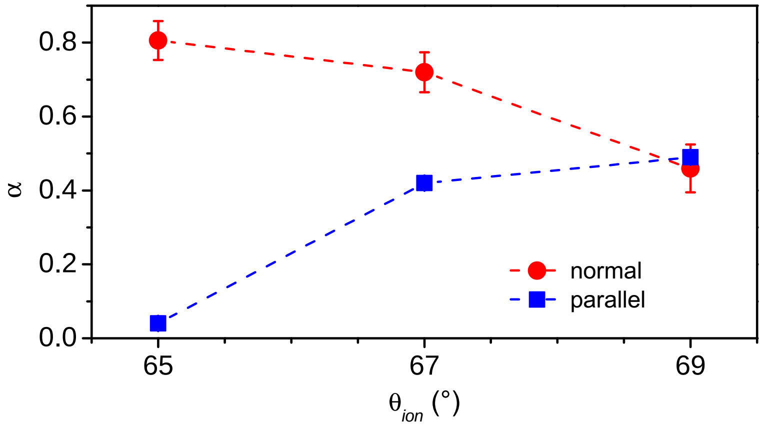

Figure 6.12: Roughness exponents for all three incident angles in the direction normal and parallel to the ion beam, respectively.

same experimental conditions from *ex-situ* AFM, $\alpha_n = 0.76 \pm 0.04$ and $\alpha_p = 0.41 \pm 0.04$, as shown in section 6.2.

Fig. 6.12 summarizes the determined values of the roughness exponents $\alpha_{n,p}$ for the three incident angles. At $\theta_{ion} = 65°$, a strong scaling anisotropy is observed with $\alpha_n = 0.81 \pm 0.05$ and $\alpha_p = 0.04 \pm 0.02$. At $\theta_{ion} = 67°$, however, this anisotropy is substantially reduced, and at $\theta_{ion} = 69°$, the scaling of the surface becomes isotropic with $\alpha_p \approx \alpha_n = 0.46 \pm 0.07$.

The two-dimensional interface width w has been calculated from the total integrated scattering (TIS) according to equation (5.3). Fig. 6.13(a) shows the evolution of w (normalized to the interface width w_0 of the the virgin substrate) for the three angles under investigation. The relative interface width increases roughly with the power of the fluence and is similar for all angles. The growth exponent β is approximately 0.20 for all three angles. The evolution of the ripple wavelength λ, as determined from the position of the local maxima of the S_p curves of all three angles, is depicted in Fig. 6.13(b). Within the experimental errors, the same absolute values and time dependencies are observed. The determined coarsening exponent is $n \approx 0.09$.

Slight variations of the incident angle by $\Delta\theta_{ion} = \pm 2°$ do neither influence the rough-

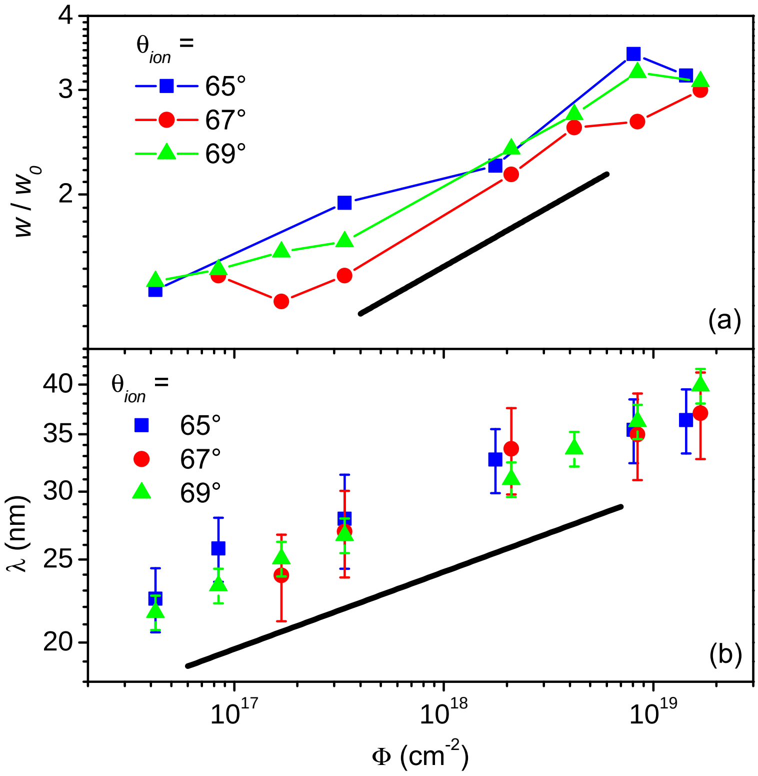

Figure 6.13: Evolution of the normalized interface width w/w_0 (a) and the ripple wavelength λ (b) for all three incident angles. The thick lines correspond to power law dependencies with a growth exponent $\beta = 0.2$ (a) and a coarsening exponent $n = 0.09$ (b), respectively.

ening dynamics of the surface nor the coarsening of the ripple wavelength. However, the roughness exponents are strongly affected by these small variations. The observed transition from anisotropic to isotropic scaling can be interpreted in terms of equilibrium phase transitions [75]. At $\theta_{ion} = 69°$, the system is neatly balanced at a fixed point similar to the critical point in equilibrium systems [41]. In this fixed point, the anisotropy exponents $\chi_x = \chi_y = 1$ (see chapter 4.4) with the critical roughness exponents becoming $\alpha_p \approx \alpha_n = 0.46 \pm 0.07$. A slight variation of the incident angle (analogous to the temperature in equilibrium phase transitions) will lead to a detuning of the system and cause it to get attracted no longer by this fixed point but by another one. For $65^\circ \leq \theta_{ion} < 69^\circ$, the system seems to be attracted to an anisotropic fixed point with anisotropic critical exponents and $\chi_x \neq \chi_y$. However, since a rather smooth transition from isotropic to anisotropic scaling is observed, the measured anisotropic roughness exponents are probably not the critical exponents of this fixed point but intermediate ones that will further change with increasing time as the system approaches its asymptotic state. Nevertheless, this observation indicates the presence of at least two different fixed points, an isotropic and an anisotropic one, in this experimental system.

For the isotropic stochastic KS equation in 2+1 dimensions that corresponds to normal ion incidence, analytical [42] and numerical [42, 102] studies indicate the existence of two different fixed points: a KPZ and an EW fixed point. Based on general considerations [24], the presence of such an isotropic EW and an isotropic KPZ fixed point is expected also in the anisotropic KS equation. In the case of its generalizations (cf. chapter 2.3), however, the number of fixed points and the values of their corresponding critical exponents are still to be investigated. Nevertheless, one should note that the experimentally measured isotropic exponents $\alpha_{n,p} = 0.46 \pm 0.07$ and $\beta \approx 0.20 \pm 0.06$ for 69° ion incidence agree reasonably well with those of the isotropic KPZ equation, $\alpha_{KPZ} = 0.38$ and $\beta_{KPZ} = 0.24$. This might indicate the existence of such an isotropic KPZ fixed point also in off-normal ion erosion systems. Since the results of the *ex-situ* AFM investigation presented in the previous section strongly support the hydrodynamic model of ion erosion as a potential continuum description for the present experimental system, the existence of such an isotropic fixed point can be used as a criterion for the verification of this assumption. For this, however, future theoretical work is required in order to explore the dynamic scaling behavior of this rather complex model.

Chapter 7

Conclusions

In this work, the evolution of amorphous surfaces during low-energy ion sputtering at oblique incident angles has been studied in experiment and simulation. The temporal surface evolution can be divided in two regimes. In the linear regime at short sputter times, ordered ripple patterns form by self-organization and grow in amplitude. Then, at longer times, a transition to a nonlinear regime occurs in which the ripple amplitude saturates. The investigation of the surface evolution in this nonlinear regime was the main focus of this work.

Since the various continuum models of ion erosion are quite well studied in the isotropic but not in the anisotropic case, numerical integrations of the aKS equation have been performed in order to investigate the influence of anisotropy on the surface morphology. For a strong nonlinear anisotropy, a rotation of the formed ripple pattern by 90° was observed for intermediate and long integration times. A similar behavior has also been found in recent experiments on crystalline silicon surfaces performed at elevated temperature [44,53]. Comparison of the simulations with analytical predictions indicates that the observed rotated ripple pattern actually results from the fact that the renormalization of the aKS equation to the KPZ equation occurs earlier in the x than in the y-direction for such a strong nonlinear anisotropy. This could also explain above mentioned experimental observations, although the simulations are not able to reproduce the experimentally observed coarsening of the ripple wavelengths.

In addition, simulations of the anisotropic dKS equation have been performed. The isotropic dKS equation is known to successfully reproduce the formation of hexagonally ordered dot patterns but not the occasionally observed coarsening of the dots [65]. In the numerical integrations of the adKS equation presented in this work, however, coarsening of the ripples is found. This is the first observation of wavelength coarsening in the adKS equation. It appears to be a purely nonlinear anisotropy effect that occurs only in a narrow range of the nonlinear anisotropy parameter and for rather low damping values. Therefore, this coarsening effect is absent in isotropic dKS as well as in most adKS simulations. Nevertheless, this result proves the applicability of the adKS equation to systems that exhibit coarsening.

The evolution of silicon surfaces has been studied during sputtering with sub-keV Ar ions under 67° incidence at fluences up to 10^{20} cm^{-2}. At short lateral scales, *ex-situ* AFM measurements of the sputtered surfaces revealed the formation of a nanoscale ripple pattern oriented normal to the direction of the incident ion beam at low fluences. At higher fluences, this initial ripple pattern is overlayed by larger corrugations that form another ripple-like pattern oriented parallel to the beam direction at larger lateral scales. Both of these ripple patterns show similar marginal coarsening of the wavelength. At low fluences, the local interface width is determined by the ripple amplitude. At intermediate and high fluences, however, it is determined by the larger corrugations. A power-law growth of the two-dimensional local interface width is found with a growth exponent $\beta = 0.27 \pm 0.02$.

The dynamic scaling behavior of the sputtered surfaces has been investigated over the whole fluence range. The main results of this *ex-situ* dynamic scaling analysis are summarized below:

- The dynamic scaling behavior at low fluences and short lateral scales indicates the presence of a KS like instability and a linear coefficient $|\nu_n| \approx 0$ in the direction parallel and normal to the projection of the ion beam, respectively.

- At high fluences, the ripple wavelength saturates and the large scale morphology of the surface exhibits a scaling anisotropy with the roughness exponents $\alpha_n = 0.76 \pm 0.04$ and $\alpha_p = 0.41 \pm 0.04$ in the direction normal and parallel to the ion beam, respectively.

- The observed algebraic scaling behavior at high fluences and large lateral scales does not agree with the aKS equation, which is expected to exhibit isotropic logarithmic scaling [24] or rotated ripple structures [72] under the current experimental conditions.

- Although the dynamic scaling exponents of the recent hydrodynamic model [68] of ion erosion are not known yet, the observed interrupted wavelength coarsening and the anisotropic algebraic scaling indicates that this model might be able to describe the present experiments. However, it remains to be seen whether the observation that ripple coarsening continues after the saturation of the ripple amplitude can be still accommodated by the dynamics of this model [100].

In further experiments, the dynamic scaling behavior of the silicon surfaces has been studied *in-situ* during sputtering at slightly different incident angles by means of grazing incidence small angle X-ray scattering. A rather smooth transition from strongly anisotropic to isotropic scaling is observed for an increase of the incident angle from 65° to 69°. This indicates the existence of at least one isotropic and one anisotropic fixed point in this particular experimental system. The measured scaling exponents of the isotropic fixed point, $\alpha = 0.46 \pm 0.07$ and $\beta \approx 0.20 \pm 0.05$, agree reasonably well with those of the isotropic KPZ equation. Since the isotropic KS equation is expected to exhibit an isotropic KPZ fixed point [42], this result might indicate the presence of such a fixed point also in anisotropic erosion systems and could, therefore, be used in future works for the verification of the assumption that the hydrodynamic model describes this particular experimental system.

Bibliography

[1] Navez, M., Sella, C., and Chaperot, D. *C. R. Acad. Sci. Paris* **254**, 240 (1962).

[2] Lewis, G. W., Nobes, M. J., Carter, G., and Whitton, J. L. *Nucl. Inst. Meth. Phys. Res. B* **170**, 363 (1980).

[3] Carter, G., Nobes, M. J., Paton, F., Williams, J. S., and Whitton, J. L. *Radiat. Eff. Defects Solids* **33**(2), 65 (1977).

[4] Vasiliu, F., Teodorescu, I. A., and Glodeanu, F. *J. Mater. Sci.* **10**, 399 (1975).

[5] Erlebacher, J., Aziz, M. J., Chason, E., Sinclair, M. B., and Floro, J. A. *Phys. Rev. Lett.* **82**(11), 2330 (1999).

[6] Chason, E., Mayer, T. M., Kellerman, B. K., McIlroy, D. T., and Howard, A. J. *Phys. Rev. Lett.* **72**(19), 3040 (1994).

[7] Rusponi, S., Costantini, G., Boragno, C., and Valbusa, U. *Phys. Rev. Lett.* **81**(13), 2735 (1998).

[8] Carter, G. and Vishnyakov, V. *Phys. Rev. B* **54**(24), 17647 (1996).

[9] Fascko, S., Dekorsy, T., Koerdt, C., Trappe, C., Kurz, H., Vogt, A., and Hartnagel, H. *Science* **285**, 1551 (1999).

[10] Gago, R., Vázquez, L., Cuerno, R., Varela, M., Ballesteros, C., and Albella, J. M. *Appl. Phys. Lett.* **78**, 3316 (2001).

[11] Frost, F., Schindler, A., and Bigl, F. *Phys. Rev. Lett.* **85**(19), 4116 (2000).

[12] Ziberi, B., Frost, F., and Rauschenbach, B. *App. Phys. Lett.* **88**, 173115 (2006).

[13] Smirnov, V. K., Kibalov, D. S., Orlov, O. M., and Graboshnikov, V. V. *Nanotechnology* **14**, 709 (2003).

[14] Mussi, V., Granone, F., Boragno, C., de Mongeot, F. B., Valbusa, U., Dodecaneso, V., Marolo, T., and Montereali, R. M. *App. Phys. Lett.* **88**, 103116 (2006).

[15] Mussi, V., Montereali, R. M., Nichelatti, E., Boragno, C., de Mongeot, F. B., and Valbusa, U. *Surf. Sci.* **601**(13), 2746 (2007).

[16] Bobek, T., Mikuszeit, N., Camarero, J., Kyrsta, S., Yang, L., Niño, M. A., Hofer, C., Gridneva, L., Arvanitis, D., Miranda, R., de Miguel, J. J., Teichert, C., and Kurz, H. *Adv. Mat.* **19**, 4375 (2007).

[17] Bobek, T. and Kurz, H. *Nucl. Inst. Meth. Phys. Res. B* **257**, 771 (2007).

[18] Bisio, F., Moroni, R., de Mongeot, F. B., Canepa, M., and Mattera, L. *Phys. Rev. Lett.* **96**, 057204 (2006).

[19] Liedke, M. O., Liedke, B., Keller, A., Hillebrands, B., Mücklich, A., Facsko, S., and Fassbender, J. *Phys. Rev. B* **75**(22), 220407(R) (2007).

[20] Oates, T. W. H., Keller, A., Facsko, S., and Mücklich, A. *Plasmonics* **2**(2), 47 (2007).

[21] Oates, T. W. H., Keller, A., Noda, S., and Facsko, S. *Appl. Phys. Lett* **93**, 063106 (2008).

[22] Bradley, R. M. and Harper, J. M. E. *J. Vac. Sci. Technol. A* **6**(4), 2390 (1988).

[23] Sigmund, P. *J. Mater. Sci.* **8**, 1545 (1973).

[24] Cuerno, R. and Barabási, A.-L. *Phys. Rev. Lett.* **74**, 4746 (1995).

[25] Park, S., Kahng, B., Jeong, H., and Barabási, A.-L. *Phys. Rev. Lett.* **83**(17), 3486 (1999).

[26] Cuerno, R., Makse, H. A., Tomassone, S., Harrington, S. T., and Stanley, H. E. *Phys. Rev. Lett.* **75**(24), 4464 (1995).

[27] Habenicht, S., Bolse, W., Lieb, K. P., Reimann, K., and Geyer, U. *Phys. Rev. B* **60**(4), R2200 (1999).

[28] Bobek, T., Facsko, S., Kurz, H., Dekorsy, T., Xu, M., and Teichert, C. *Phys. Rev. B* **68**, 085324 (2003).

[29] Ziberi, B., Frost, F., Höche, T., and Rauschenbach, B. *Phys. Rev. B* **72**, 235310 (2005).

[30] Rusponi, S., Costantini, G., Boragno, C., and Valbusa, U. *Phys. Rev. Lett.* **81**(19), 4184 (1998).

[31] Alkemade, P. F. A. and Jiang, Z. X. *J. Vac. Sci. Technol. B* **19**(5), 1699 (2001).

[32] Datta, D. P. and Chini, T. K. *Phys. Rev. B* **69**, 235313 (2004).

[33] Datta, D. P. and Chini, T. K. *Phys. Rev. B* **76**, 075323 (2007).

[34] Makeev, M. A., Cuerno, R., and Barabási, A.-L. *Nucl. Inst. Meth. Phys. Res. B* **197**, 185 (2002).

[35] Facsko, S., Bobek, T., Stahl, A., Kurz, H., and Dekorsy, T. *Phys. Rev. B* **69**, 153412 (2004).

[36] Aste, T. and Valbusa, U. *New J. Phys.* **7**, 122 (2005).

[37] Castro, M., Cuerno, R., Vázquez, L., and Gago, R. *Phys. Rev. Lett.* **94**, 016102 (2005).

[38] Muñoz-García, J., Castro, M., and Cuerno, R. *Phys. Rev. Lett.* **96**, 086101 (2006).

[39] Barabási, A.-L. and Stanley, H. E. *Fractal Concepts in Surface Growth.* Cambridge University Press, (1995).

[40] Stanley, H. E. *Phase Transitions and Critical Phenomena.* Oxford University Press, (1971).

[41] Plischke, M. and Bergersen, B. *Equilibrium Statistical Physics.* World Scientific, (2006).

[42] Cuerno, R. and Lauritsen, K. B. *Phys. Rev. E* **52**(5), 4853 (1995).

[43] Ziberi, B., Frost, F., Tartz, M., Neumann, H., and Rauschenbach, B. *Appl. Phys. Lett.* **92**, 063102 (2008).

[44] Brown, A.-D., Erlebacher, J., Chan, W.-L., and Chason, E. *Phys. Rev. Lett* **95**, 056101 (2005).

[45] Gnaser, H. *Low Energy Ion Irradiation of Solid Surfaces.* Springer-Verlag New York, Inc, 1. edition, (1998).

[46] Sigmund, P. *Phys. Rev.* **184**(2), 383 (1969).

[47] Flamm, D., Frost, F., and Hirsch, D. *Appl. Surf. Sci.* **179**, 95 (2001).

[48] Karmakar, P. and Ghose, D. *Surf. Sci.* **554**, L101 (2004).

[49] Erlebacher, J., Aziz, M. J., Chason, E., Sinclair, M. B., and Floro, J. A. *J. Vac. Sci. Technol. A* **18**(1), 115 (2000).

[50] Chason, E., Erlebacher, J., Aziz, M. J., Floro, J. A., and Sinclair, M. B. *Nucl. Inst. Meth. Phys. Res. B* **178**, 55 (2001).

[51] Ziberi, B., Frost, F., and Rauschenbach, B. *J. Vac. Sci. Technol. A* **24**(4), 1344 (2006).

[52] Chan, W. L. and Chason, E. *J. Appl. Phys.* **101**, 121301 (2007).

[53] Brown, A.-D. and Erlebacher, J. *Phys. Rev. B* **72**, 075350 (2005).

[54] Habenicht, S. *Phys. Rev. B* **63**, 125419 (2001).

[55] Chini, T. K., Sanyal, M. K., and Bhattacharyya, S. R. *Phys. Rev. B* **66**, 153404 (2002).

[56] MacLaren, S. W., Baker, J. E., Finnegan, N. L., and Loxton, C. M. *J. Vac. Sci. Technol. A* **10**(3), 468 (1992).

[57] Umbach, C. C., Headrick, R. L., and Chang, K.-C. *Phys. Rev. Lett.* **87**(24), 246104 (2001).

[58] Kardar, M., Parisi, G., and Zhang, Y.-C. *Phys. Rev. Lett.* **56**(9), 889 (1986).

[59] Kuramoto, Y. and Tsuzuki, T. *Prog. Theor. Phys.* **55**, 356 (1976).

[60] Sivashinsky, G. I. *Acta Astronaut.* **6**, 569 (1979).

[61] Paniconi, M. and Elder, K. R. *Phys. Rev. E* **56**(3), 2713 (1997).

[62] Buceta, J., Pastor, J., Rubio, M. A., and de la Rubia, F. J. *Physica A* **113**, 166 (1998).

[63] Vogel, S. and Linz, S. J. *Phys. Rev. B* **752**, 035416 (2005).

[64] Vogel, S. and Linz, S. J. *Europhys. Lett.* **76**(5), 884 (2006).

[65] Vogel, S. and Linz, S. J. *Phys. Rev. B* **75**, 085425 (2007).

[66] Vogel, S. and Linz, S. J. *Phys. Rev. B* **75**, 155417 (2007).

[67] Makeev, M. A. and Barabási, A.-L. *Appl. Phys. Lett.* **71**(19), 2800 (1997).

[68] Muñoz-García, J., Cuerno, R., and Castro, M. *Phys. Rev. B* **78**, 205408 (2008).

[69] Muñoz-García, J., Cuerno, R., and Castro, M. *Phys. Rev. E* **74**, 050103(R) (2006).

[70] Drotar, J., Zhao, Y.-P., Lu, T.-M., and Wang, G.-C. *Phys. Rev. E* **59**(1), 177 (1999).

[71] Sneppen, K., Krug, J., Jensen, M. H., Jayaprakash, C., and Bohr, T. *Phys. Rev. A* **46**(12) (1992).

[72] Rost, M. and Krug, J. *Phys. Rev. Lett* **75**(21), 3894 (1995).

[73] Kim, J., Kahng, B., and Barabási, A.-L. *Appl. Phys. Lett.* **81**(19), 3654 (2002).

[74] Lam, C.-H. and Shin, F. G. *Phys. Rev. E* **58**(5), 5592 (1998).

[75] Cuerno, R. *private communication.*

[76] Habenicht, S., Lieb, K. P., Koch, J., and Wieck, A. D. *Phys. Rev. B* **65**, 115327 (2002).

[77] Meakin, P. *Phys. Rep.* **235**, 198 (1993).

[78] Halpin-Healy, T. and Zhang, Y.-C. *Phys. Rep.* **254**, 215 (1995).

[79] Vicsek, T. and Family, F. *Phys. Rev. Lett.* **52**(19), 1669 (1984).

[80] Lopez, J. M., Rodríguez, M. A., and Cuerno, R. *Physica A* **246**, 329 (1997).

[81] Ramasco, J. J., López, J. M., and Rodríguez, M. A. *Phys. Rev. Lett.* **84**(10), 2199 (2000).

[82] Pastor-Satorras, R. and Rothman, D. H. *Phys. Rev. Lett.* **80**(19), 4349 (1998).

[83] Pastor-Satorras, R. and Rothman, D. H. *J. Stat. Phys.* **93**(3/4), 477 (1998).

[84] Schmittmann, B., Pruessner, G., and Janssen, H.-K. *Phys. Rev. E* **73**, 051603 (2006).

[85] Roßbach, S. *Nanostrukturierung von Silizium-Oberflächen durch atomare Erosion.* Diploma thesis, Fachbereich Elektrotechnik, Westsächsische Hochschule Zwickau (FH), Germany, (2006).

[86] Kaufman, H. R. *J. Vac. Sci. Technol.* **15**(2), 272 (1978).

[87] Wolf, B., editor. *Handbook of Ion Sources.* CRC Press, (1995).

[88] Wolf, G. K., Zucholl, K., Barth, M., and Ensinger, W. *Nucl. Inst. Meth. Phys. Res. B* **21**, 570 (1987).

[89] Frost, F., Fechner, R., Ziberi, B., Flamm, D., and Schindler, A. *Thin Solid Films* **459**, 100 (2004).

[90] Binnig, G., Quate, C. F., and Gerber, C. *Phys. Rev. Lett.* **86**(9), 930 (1986).

[91] Giessibl, F. J. *Rev. Mod. Phys.* **75**(3), 949 (2003).

[92] Wiesendanger, R. *Scanning Probe Microscopy and Spectroscopy: Methods and Applications.* Cambridge University Press, (1995).

[93] Howland, R. and Benatar, L. *A Practical Guide to Scanning Probe Microscopy.* ThermoMicroscopes, (2000).

[94] Peverini, L., Ziegler, E., and Kozhevnikov, I. *Appl. Phys. Lett.* **91**, 053121 (2007).

[95] Peverini, L. *Study of the processes of layer growth and ion beam etching using specular and diffuse X-ray scattering.* PhD thesis, University Joseph Fourier, Grenoble, France, (2005).

[96] Jiang, Z. X. and Alkemade, P. F. A. *App. Phys. Lett.* **75**(3), 315 (1998).

[97] Zhang, K., Rotter, F., Uhrmacher, M., Ronning, C., Hofsäss, H., and Krauser, J. *Surf. Coat. Technol.* **201**, 8299 (2007).

[98] Gago, R., Vázquez, L., Cuerno, R., Varela, M., Ballesteros, C., and Albella, J. M. *Nanotechnology* **12**, 304 (2002).

[99] Carter, G. *J. Appl. Phys.* **85**, 455 (1999).

[100] Keller, A., Cuerno, R., Facsko, S., and Möller, W. *Phys. Rev. B* **79**, 115437 (2009).

[101] Muñoz-García, J., Vázquez, L., Cuerno, R., Sánchez-García, J. A., Castro, M., and Gago, R. In *Toward Functional Nanomaterials,* Wang, Z. M., editor. Springer, New York (2009).

[102] Tok, E. S., Ong, S. W., and Kang, H. C. *Phys. Rev. E* **70**, 011604 (2004).

Acknowledgements

This thesis wouldn't have been possible without the support and help of quite some people.

Special thanks go to my supervisor and friend Stefan Facsko for his great support and continuous encouragement, for the countless hours we spent in his office talking about everything under the sun, and for teaching me the Rules Of The Game. I owe you big time.

Many thanks to Wolfhard Möller and Martin Springer for their support of and during the project "Dr. rer. nat."

It is a particular pleasure for me to thank Rodolfo Cuerno for reviewing this thesis, as well as for all the discussions, comments, suggestions, and explanations, and especially for giving me the opportunity to spend four weeks in Madrid. I had a great time there, I learned a lot, and I guess I still owe you quite some beers.

I also wish to thank Luca Peverini and Igor Kozhevnikov for the experimental support at the ESRF and the help with the data analysis.

Thanks go to Oskar Liedke for help with the AFM.

Thanks also to the members of the Ion Beam Analysis department for the discussions and the technical and experimental support.

And to all the others who are not listed here but contributed to the success of this work in one way or another, well, you guys know who you are and you know that I owe you one.

You know what? Here's my actual true . . . I've had a vision. And what it is, is although this is a world where good men are murdered in their prime, and mediocre hacks thrive and proliferate, I gotta share this with ya, cos I love you and you feel that. You know all that money we spend on nuclear weapons and defence every year? Trillions of dollars? Correct? *Trillions.* Instead, if we spent that money feeding and clothing the poor of the world, which it would pay for many times over, not *one* human being excluded, not *one*, we could, as one race, explore outer space in peace for ever. You've been great, thank you.

BILL HICKS, 1990

List of publications

Parts of this work have been published in:

Anisotropic scaling of ripple morphologies on high-fluence sputtered silicon
A. Keller, R. Cuerno, S. Facsko, and W. Möller,
Physical Review B **79**, 115437 (2009)

Simultaneous formation of two ripple modes on ion sputtered silicon
A. Keller, S. Roßbach, S. Facsko, and W. Möller,
Nanotechnology **19**, 135303 (2008)

Other publications:

Introducing artificial length scales to tailor magnetic properties
J. Fassbender, T. Strache, M.O. Liedke, D. Marko, S. Wintz, K. Lenz, A. Keller, S. Facsko, I. Mönch, and J. McCord,
New Journal of Physics (2009), in press

Transition from smoothing to roughening of ion-eroded GaSb sufaces
A. Keller, A. Biermanns, G. Carbone, J. Grenzer, S. Facsko, O. Plantevin, R. Gago, and T.H. Metzger,
Applied Physics Letters **94**, 193103 (2009)

Evolution of ion-induced ripple patterns on SiO_2 surfaces
A. Keller, S. Facsko, and W. Möller,
Nuclear Instruments and Methods in Physics Research B **267**, 656 (2009)

Self-organized metallic nanoparticle and nanowire arrays from ion-sputtered silicon

templates
T.W.H. Oates, A. Keller, S. Noda, and S. Facsko,
Applied Physics Letters **93**, 063106 (2008)

Minimization of topological defects in ion-induced ripple patterns on silicon
A. Keller, S. Facsko, and W. Möller,
New Journal of Physics **10**, 063004 (2008)

Induced anisotropies in exchange coupled systems on rippled substrates
M.O. Liedke, B. Liedke, A. Keller, B. Hillebrands, A. Mücklich, S. Facsko, and J. Fassbender,
Physical Review B **75**, 220407(R) (2007)

Aligned silver nanoparticles on rippled silicon templates exhibiting anisotropic plasmon absorption
T.W.H. Oates, A. Keller, S. Facsko, and A. Mücklich,
Plasmonics **2**, 47 (2007)

Interaction of highly charged ions with insulator surfaces
S. Facsko, D. Kost, A. Keller, W. Möller, Z. Pešić, and N. Stolterfoht,
Radiation Physics and Chemistry **76**, 387 (2007)

Versicherung

Hiermit versichere ich, dass ich die vorliegende Arbeit ohne unzulässige Hilfe Dritter und ohne Benutzung anderer als der angegebenen Hilfsmittel angefertigt habe; die aus fremden Quellen direkt oder indirekt übernommenen Gedanken sind als solche kenntlich gemacht. Die Arbeit wurde bisher weder im Inland noch im Ausland in gleicher oder ähnlicher Form einer anderen Prüfungsbehörde vorgelegt.
Ich erkenne die Promotionsordnung der Technischen Universität Dresden an.

Dresden, 10.03.2009

Adrian Keller

Diese Arbeit wurde am Forschungszentrum Dresden-Rossendorf e.V. und unter wissenschaftlicher Betreuung von Dr. Stefan Facsko und Prof. Dr. Wolfhard Möller angefertigt.
Wolfhard Möller ist Professor im Institut für Angewandte Physik der Fakultät Mathematik und Naturwissenschaften der Technischen Universität Dresden.